The Influence of Wind on Internal Solitary Waves

by

Chichi Zhou

A thesis
presented to the University of Waterloo
in fulfillment of the
thesis requirement for the degree of
Master of Mathematics
in
Applied Mathematics

Waterloo, Ontario, Canada, 2026

© Chichi Zhou 2026

Author's Declaration

I hereby declare that I am the sole author of this thesis. This is a true copy of the thesis, including any required final revisions, as accepted by my examiners.

I understand that my thesis may be made electronically available to the public.

Abstract

Internal solitary waves (ISWs) are a type of nonlinear internal wave that can propagate over long distances while maintaining their non-sinusoidal form. Their nonlinear nature makes them sensitive to changes in background conditions, such as stratification and shear currents. Commonly observed in the coastal ocean, ISWs are susceptible to the complexity of coastal ocean environments, where they may become unstable and undergo a series of evolution stages and instabilities. Wind, as an important atmospheric forcing, is widely known to induce changes in the upper ocean and therefore has the potential to affect the propagation of ISWs. However, this air-sea coupled effect has not been fully investigated. This study therefore aims to explore the effect of wind on ISW propagation.

In this thesis, we use the MITgcm model equipped with the K-Profile Parameterization (KPP) scheme to study internal solitary waves affected by strong wind. Idealized background conditions are applied to isolate wind-induced effects on the wave field. We begin by performing a series of sensitivity tests to determine the optimal numerical parameters. Numerical simulations under various wind conditions are then conducted to explore how wind direction, strength, and temporal variability in wind stress affect the propagation of internal solitary waves. The analysis focuses on wave characteristics, including amplitude, propagation speed, and the development of instabilities during wave evolution. The effects of wind on the flow field can be summarized as enhanced mixing and the induction of near-surface shear currents. The DJL equation is also introduced to examine the separate effects of these two factors in cases where numerical solutions can be obtained.

Acknowledgements

First, I would like to thank my supervisors, Dr. Marek Stastna and Dr. Kevin Lamb, for their guidance and patience. Marek is a very supportive supervisor. He is always willing to help, consistently provides constructive feedback, and genuinely cares about students. It is a pleasure to work with Marek closely over the past two years. Kevin helped me establish this thesis project during the first year with great patience, and I benefited a lot from the discussions. I am grateful to both of them for their dedication and support. I would also thank my committee members Dr. Francis Poulin and Dr. Barbara Zemskova for reading my thesis.

I would also like to thank everyone in our research group, including Nico, Leonard, Khush, Erika, and Clara (who will be joining soon!), as well as my friends in the broader fluid mechanics group, especially Rose, Joaquin, Jakob, and Jonathan, for all the academic and non-academic conversations and for the many days and even some evenings we spent together. Thank you all for creating such a friendly and welcoming environment. These experiences have become the most precious memories of my time at Waterloo, something I could never have imagined before I came here. My graduate experience would not have been nearly as memorable without all of you. I would also like to thank Alain and Derek for providing me with valuable opportunities and support, which have been greatly helpful.

My gratitude also goes to my friends across the ocean for their friendship and for always willing to talk to me despite the 12-hour time difference. I alway feel very lucky to have them in my life. I would also thank all the friends and kind people I have met here over the past nearly three years, which has made life far from home much easier.

Finally, I would like to thank my parents for their consistent care and for supporting all of my decisions. Their support has been truly invaluable.

Table of Contents

Author's Declaration ii

Abstract iii

Acknowledgements iv

List of Figures viii

List of Tables xiii

List of Abbreviations xiv

1 Introduction 1

1.1 The Coastal Ocean Environment 1

1.2 Internal Waves and Internal Solitary Waves 2

1.3 Wind Forcing and Upper Ocean Response 4

1.4 Approach to the Study of Internal Solitary Waves 6

1.5 Thesis Overview 7

2 Methods 9

2.1 Governing Equations 9

2.1.1 Basic Fluid equations under the Boussinesq Approximation 9

2.1.2 MITgcm governing equations . . . 10
2.1.3 Dimensionless Numbers . . . 11
2.2 Numerical Implementation in the MITgcm Model . . . 13
2.2.1 Overview of the Numerical Procedure . . . 13
2.2.2 Temporal Scheme . . . 14
2.2.3 Spatial Scheme . . . 15
2.3 Turbulence Closure and Vertical Mixing . . . 16
2.3.1 Reynolds decomposition and closure problem . . . 16
2.3.2 Representation of turbulent processes in the MITgcm . . . 17
2.4 Vertical Mixing Scheme: K-Profile Parameterization . . . 19
2.4.1 General Introduction . . . 19
2.4.2 General Structure of KPP Scheme . . . 22

3 Sensitivity Analysis **26**
3.1 Model Configuration and Initial Fields . . . 26
3.2 Sensitivity Tests . . . 27
3.2.1 KPP Turbulent Parameterization . . . 27
3.2.2 Grid Size . . . 31
3.2.3 Diffusion Parameters . . . 33

4 Results **35**
4.1 Introduction . . . 35
4.2 Model Configuration . . . 36
4.3 Baseline Constant Wind Stress Simulations . . . 37
4.3.1 Positive Constant Wind Stress . . . 37
4.3.2 Negative Constant Wind Stress . . . 43
4.4 Parameter Influence Experiments . . . 46
4.4.1 Wind Strength . . . 46
4.4.2 Ramp Wind . . . 49

5 Discussion and Conclusions **56**

References **61**

List of Figures

1.1 South China Sea cross-section showing bathymetry, dynamics, and processes associated with internal solitary wave activity, adapted from Fig. 3(d) of (Alford et al., 2015). 2

1.2 Distribution of high-frequency nonlinear internal waves by MODIS, observed from August 2002 through May 2004. Cited from Jackson (2007), Figure 1. 3

1.3 Schematic of dynamical processes in the upper ocean. Turbulent mixing induced by surface forcings maintains the mixed layer. Cited from Ferrari and Boccaletti (2004), Figure 1. 5

1.4 Satellite image showing internal solitary wave trains generated in the Strait of Messina and propagating southward. Alternating dark (smooth) and light (rough) surface patterns indicate the presence of ISWs. Image source: https://earthobservatory.nasa.gov/images/7630/messina-strait-italy 8

2.1 Downward propagation of momentum from wind. F_{wind} represents wind force acting only on the surface layer. τ_{xz} denotes eddy viscous shear stress that transfers the wind-induced momentum downward. Only the first three grid layers are shown. 12

2.2 Finite-volume discretization on an Arakawa C grid. Tracer variables are located at cell centres, while velocity components are located at cell faces, where the arrows indicate the corresponding flux directions. Adapted from Gelderloos et al. (2016) Fig. 1, following the MITgcm indexing convention. 15

2.3 Diagram of ocean profiles associated with the KPP boundary layer parameterization. The ocean has a total depth $H + \eta$, where η is the height of the free surface. The ocean surface is subject to external fluxes, driving turbulence within the ocean surface boundary layer (OSBL) to a depth of h. Below the OSBL is the ocean interior, where turbulence is considered to be dominated by processes including internal wave breaking, double diffusion, and shear instability. The eddy diffusivities in the OSBL and ocean interior are matched at the base of the OSBL ($z = -h$). 20

2.4 Procedure for calculating the KPP diffusivity and nonlocal transport terms in the KPP scheme. The interior diffusivity is computed first and used as a reference to ensure smooth matching of the boundary-layer diffusivity at the interface. 21

3.1 Experimental design for the sensitivity tests. The vertical mixing scheme uses either constant eddy diffusivity parameters (denoted as "constant") or KPP. Δx and Δz denote the horizontal and vertical grid sizes, respectively. A_h and A_v denote the horizontal and vertical eddy viscosity/diffusivity, respectively. 28

3.2 Sensitivity tests for Groups 1 and 3 at $t = 0.7\,\mathrm{h}$. Shading is the horizontal velocity fields, and lines are the density contours. (a)–(c) results for cases C1–C3 with constant diffusivity parameters; (d) vertical profiles of background currents for cases C1–C3; (e)–(g) results for cases K1–K3 with the KPP scheme; (h) vertical profiles of background currents for cases K1–K3. 32

3.3 Sensitivity tests for Group 2 at $t = 0.7\,\mathrm{h}$: (a)–(c) results for cases C1,C4,C5 with constant diffusivity parameters; (d) vertical profiles of background currents for cases C1,C4,C5. 32

3.4 Sensitivity tests for Group 4 at $t = 1\,\mathrm{h}$ with $\Delta z = 0.5\,\mathrm{m}$: (a) K4 ($\Delta x = 5\,\mathrm{m}$), (b) K1 ($\Delta x = 10\,\mathrm{m}$), (c) K5 ($\Delta x = 25\,\mathrm{m}$), (d) K6 ($\Delta x = 50\,\mathrm{m}$). 33

3.5 Sensitivity tests on background diffusivity for the KPP cases at $t = 1\,\mathrm{h}$: (a)-(d) Group 5 with $A_v = 10^{-5}\,\mathrm{m^2/s}$: (a) $A_h = 10^{-6}\,\mathrm{m^2/s}$ (K7), (b) $A_h = 10^{-5}\,\mathrm{m^2/s}$ (K1), (c) $A_h = 10^{-3}\,\mathrm{m^2/s}$ (K8), (d) $A_h = 10^{-1}\,\mathrm{m^2/s}$ (K9). (e)-(h) Group 6 with $A_h = 10^{-5}\,\mathrm{m^2/s}$: (e) $A_v = 10^{-6}\,\mathrm{m^2/s}$ (K10), (f) $A_v = 10^{-5}\,\mathrm{m^2/s}$ (K1), (g) $A_v = 10^{-3}\,\mathrm{m^2/s}$ (K11), (h) $A_v = 10^{-1}\,\mathrm{m^2/s}$ (K12). . . 34

4.1 Diagram illustrating the physical process of wind's influence on internal solitary waves. (a) Wind direction aligns with the wave propagation direction. (b) Wind direction opposes the wave propagation direction. 36

4.2 The wind patterns in P1, P1-up and P1-up-down. 37

4.3 Evolution process for Case P1 with constant $\tau_x = 0.3$ N/m^2: (a)-(e) The horizontal component of velocity u in the top 150 m is shaded, with five density contours shown in black at $t = 0$ h, 0.8 h, 1.8 h, 2.7 h, and 3.7 h. (f) The vertical profile of the wind-driven background current U_b, obtained by sampling u at $x = 35$ km; the black line represents the initial state. (g) The vertical profile of u_c at the trough of the leading wave at the same times as in (f); the blue dots represent the location where $u = c$. 38

4.4 A close-up view of the snapshot of u from $t = 0$ to $t = 1.2$ h in the top 60 m, showing only the density contours near the surface. The white lines indicate where $u = c$ and are used as a simple measure of the core thickness d_c. 40

4.5 Evolution of key characteristics in Cases P1, P2, and P3: (a) maximum amplitude $|A_{max}|$, (b) core thickness d_c, (c) propagation speed c. 41

4.6 Evolution process for Case N1 with constant $\tau_x = -0.3$ N/m^2: (a)-(e) The horizontal component of velocity u in the top 150 m is shaded, with five density contours shown in black at $t = 0$ h, 0.8 h, 1.8 h, 2.7 h, and 3.7 h. (f) The vertical profile of the wind-driven background current U_b, obtained by sampling u at $x = 35$ km; the black line represents the initial state. (g) The vertical profile of u_c at the trough of the leading wave at the same times as in (f). 42

4.7 DJL solutions at the leading wave centre under conditions C1-C4 and MITgcm solutions under N1. (a) Velocity profiles at the wave centre $u_c(z)$ at $t = 0.3$ h. (b) Same as (a), but at $t = 2.8$ h. (c) Background velocity profiles U_b at $x = 35$ km (a region without waves) from the MITgcm at $t = 0.3$ h and $t = 2.8$ h, with the fitted background velocity profiles used in DJL cases C1 and C3 superimposed. In DJL cases C2 and C4, $U_b(z) = 0$ and is not shown. (d) Density profiles at the wave centre $\rho_c(z)$ at $t = 0.3$ h. (e) Same as (d), but at $t = 2.8$ h. (f) Background density profiles ρ_b from the MITgcm at $t = 0.3$ h and $t = 2.8$ h, with the interpolated background density profiles used in DJL cases C1 and C2 superimposed. In DJL cases C3 and C4, background density profile is the initial density profile applied in MITgcm and not shown. 44

4.8 DJL solutions under conditions C1-C3 and the MITgcm solution for the temporal evolution of (a) the propagation speed c and (b) the amplitude of leading wave $|A|$. 45

4.9 Evolution process for Case P2 with constant $\tau_x = 0.6$ N/m^2: (a)-(e) The horizontal component of velocity u in the top 150 m is shaded, with five density contours shown in black at $t = 0$ h, 0.8 h, 1.8 h, 2.7 h, and 3.7 h. (f) The vertical profile of the wind-driven background current U_b, obtained by sampling u at $x = 35$ km; the black line represents the initial state. (g) The vertical profile of u_c at the trough of the leading wave at the same times as in (f); the blue dots represent the location where $u = c$. 47

4.10 Evolution process for Case P3 with constant $\tau_x = 0.15$ N/m^2: (a)-(e) The horizontal component of velocity u in the top 150 m is shaded, with five density contours shown in black at $t = 0$ h, 0.8 h, 1.8 h, 2.7 h, and 3.7 h. (f) The vertical profile of the wind-driven background current U_b, obtained by sampling u at $x = 35$ km; the black line represents the initial state. (g) The vertical profile of u at the wave trough of the leading wave at the same times as in (f); the blue dots represent the location where $u = c$. 48

4.11 Comparison of the evolution of background conditions (a) U_b^0, the velocity of wind-driven currents at the surface; and (b) MLD, the mixed layer depth diagnosed using $T - T_b^0 = -0.2$ °C. The blue, red, and orange lines represent cases P1, P1-up, and P1-up-down, respectively. 51

4.12 Comparison of cases P1-up and P1. The horizontal velocity component u in the top 150 m is shaded, with five density contours shown. Panels (a)-(d) show results from case P1-up at $t = 0.5, 0.7, 0.8, 1.0$ h. Panels (e)-(h) show results from case P1 at the same times. Panels (i)-(l) show the difference in u between the two cases, defined as $u_{\text{P1-up}} - u_{\text{P1}}$, after alignment by x_c. . . 52

4.13 Comparison of cases P1-up and P1-up-down. The horizontal velocity component u in the top 150 m is shaded, with five density contours shown. Panels (a)-(e) show results from case P1-up at $t = 3.8, 4.0, 4.2, 4.3, 4.5$ h, while panels (f)-(j) show results from case P1-up-down at the same times. . 53

4.14 Evolution of the background conditions in Case P1-up-down: (a) background current profiles, $U_b(z)$; (b) background density profiles, $\rho_b(z)$; and (c) time evolution of wind stress, τ_x, with the times selected in panels (a) and (b) marked by dots. 54

4.15 Same as Fig. 4.14, but for Case P1-up. 55

4.16 Close-up view of case P1-up-down during the wind-weakening period. Panels (a1)–(f1) show snapshots of u at $t = 3.7, 3.8, 4.0, 4.2, 4.3$, and 4.5 h in the upper 60 m, showing only the density contours near the surface as black lines. The white lines indicate where $u = c$. Panels (a2)–(f2) show the horizontal velocity profiles at the wave centre, u_c, with units of m/s. . . . 55

List of Tables

2.1 Summary of temporal treatments used in the model configuration. 14

3.1 List of sensitivity runs and parameter settings 29
3.2 List of vertical grids for sensitivity runs 30

4.1 List of runs and parameter settings 39

List of Abbreviations

DJL Dubreil-Jacotin-Long 6, 27, 36, 41, 43, 45

FVCOM Finite Volume Community Ocean Model 6

FVM Finite Volume Method 13–15

HYCOM HYbrid Coordinate Ocean Model 19

ISW internal solitary wave 2–4, 6, 7, 35–37, 39, 45, 46, 49, 57–60

KdV Korteweg-de Vries 6

KPP K-Profile Parameterization 6, 7, 15, 19, 22–24, 30, 31, 33, 36, 45, 56, 57, 59, 60

MCC Miyata-Choi-Camassa 6

MITgcm Massachusetts Institute of Technology general circulation model 6, 7, 10, 11, 13, 14, 18, 19, 26, 28, 33, 41, 43, 45, 46, 56

MLD Mixed Layer Depth 49

OSBL ocean surface boundary layer 19, 23, 24

RANS Reynolds-Averaged Navier-Stokes 17

ROMS Regional Ocean Modeling System 19

TKE turbulent kinetic energy 17–19

Chapter 1

Introduction

1.1 The Coastal Ocean Environment

The coastal ocean refers to the region extending from the shoreline to the outer edge of the continental shelf. Although it represents only a small portion of the global ocean, this region supports a wide range of human activities, including commercial shipping, fisheries, and offshore wind energy, due to its proximity to land and abundant natural resources.

One key characteristic of the coastal ocean is its complex bathymetry. Moving from the deep ocean toward the land, the seafloor transitions from the steep continental slope (typically 2–4°) to the shelf break (commonly at depths of 100–200 m), and finally to the gently sloping continental shelf that connects to the shore (Cacchione et al., 2002). Another important feature is stratification, characterized by vertical variations in density caused by changes in temperature, salinity, and pressure. The typical vertical density structure consists of three main layers: a surface mixed layer of nearly uniform density, a strongly stratified pycnocline, and a weakly stratified deep layer (Gregg, 2021).

A wide range of physical drivers, such as wind, surface waves, tides, and internal waves, are active in the coastal ocean. These processes interact with each other and with the underlying bathymetry, creating a highly dynamic environment. For example, wind-driven coastal upwelling transports cold, nutrient-rich water from the deep layers to the surface along continental margins. Through such processes, coastal oceans play an important role in biogeochemical cycling and global carbon budgets (Cai, 2011; Mathis et al., 2022; Regnier and Ciais, 2013).

Understanding the physical processes that shape the coastal ocean is essential for accurately representing ocean dynamics and for supporting marine ecosystems and human

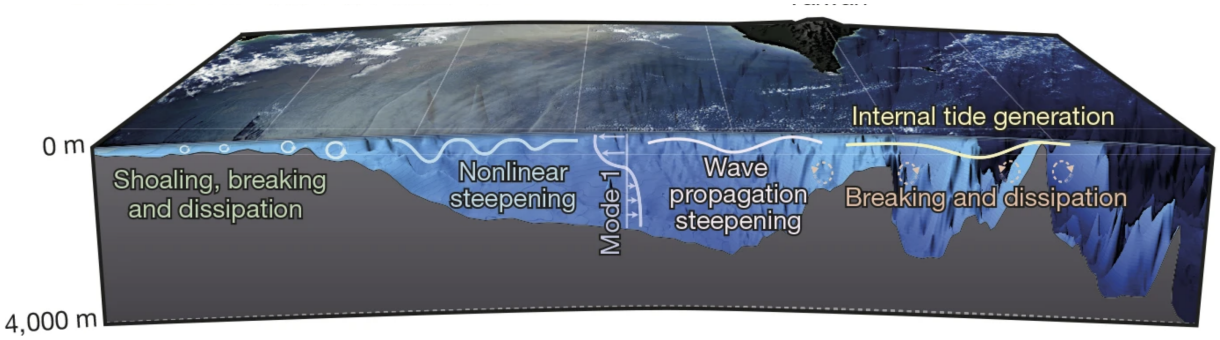


Figure 1.1: South China Sea cross-section showing bathymetry, dynamics, and processes associated with internal solitary wave activity, adapted from Fig. 3(d) of (Alford et al., 2015).

activities that rely on them.

1.2 Internal Waves and Internal Solitary Waves

Internal waves are gravity waves (i.e. waves for which the restoring force is gravity) in the ocean interior, where density stratification provides the buoyancy restoring force. They are crucial for closing the global ocean energy budget (Kunze, 2017), maintaining thermohaline circulation (Munk and Wunsch, 1998), and influencing the Earth's climate system (Whalen et al., 2020).

Internal solitary waves (ISWs), which are the focus of this study, are strongly nonlinear internal waves that propagate in the form of bell–shaped (non-sinusoidal) waves with permanent form. ISWs are frequently observed in coastal oceans (Jackson, 2007), with a map of their occurrence shown in Figure 1.2. According to Lamb et al. (2019), ISWs in the coastal ocean typically exhibit vertical displacements on the order of $O(10)$ m, with horizontal wavelengths around $O(100)$ m. Owing to their large amplitudes, ISWs are often associated with intense shear layers near the pycnocline, posing potential risks to underwater infrastructure (Chen et al., 2023; Zou et al., 2020) and vehicles (Zhao et al., 2025).

ISWs are generated by several mechanisms, the most prevalent of which is the nonlinear-dispersive transformation of internal tides (Gerkema and Zimmerman, 1995). In this process, internal tides propagate into shallower water, where nonlinear steepening transforms

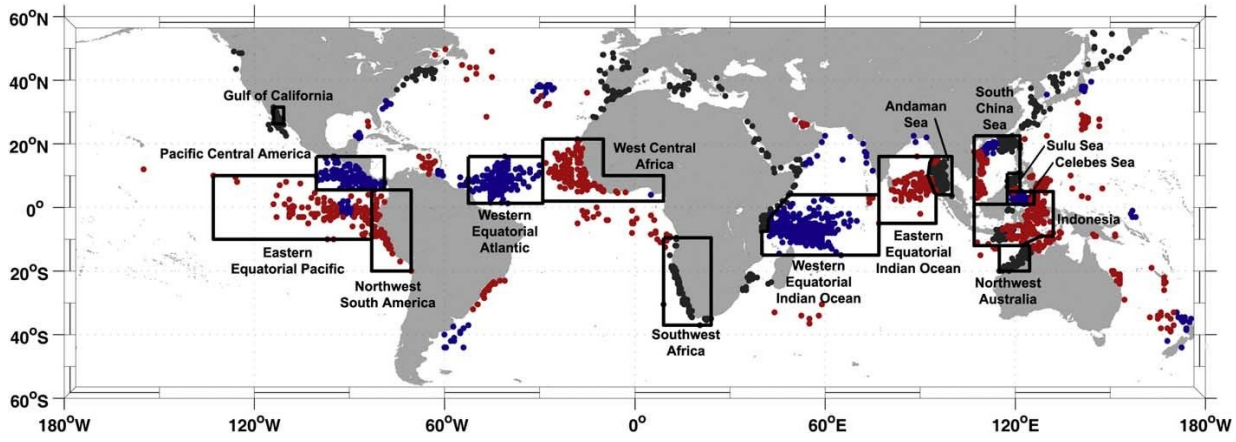


Figure 1.2: Distribution of high-frequency nonlinear internal waves by MODIS, observed from August 2002 through May 2004. Cited from Jackson (2007), Figure 1.

them into trains of solitary waves. ISWs can also form as lee waves downstream of submarine ridges and sills (Apel et al., 1985). Once generated, they can travel long distances with minimal distortion, governed by a balance between nonlinearity and dispersion.

As ISWs propagate toward the shore and encounter decreasing water depth, which is known as shoaling, they may steepen, break, or undergo fission into wave trains. The features and complexity of this process have been reviewed by Stastna and Legare (2024), emphasizing how ISW behavior is influenced by factors such as stratification, bathymetry, and background shear. Shoaling-related dynamics have been widely studied, particularly in the South China Sea, where the Luzon Strait serves as one of the primary generation regions for ISWs (Cai et al., 2012; Guo and Chen, 2014). Mixing is one important result of shoaling and it arises from four mechanisms as concluded in Lamb and Farmer (2011): wave breaking (Lamb, 2013), shear instabilities Lamb and Farmer (2011), bottom boundary layer interactions (Boegman and Stastna, 2019), and the formation of trapped core structures (Stastna and Legare, 2024), with the latter two also facilitating both vertical and horizontal material transport. These processes alter the physical and chemical environment of the coastal ocean, including nutrient distribution, sediment resuspension, and temperature structure, thereby influencing ecosystem structure and biological productivity.

1.3 Wind Forcing and Upper Ocean Response

The coastal ocean is continuously influenced by various surface processes, including wind, freshwater input, surface heat exchange, sea ice formation and melting, and other related processes. These forcings alter the fluxes of momentum, heat, and salinity at the ocean surface (Large and Pond, 1981; Price et al., 1986; Yu and Weller, 2007), thereby driving turbulent mixing in the ocean mixed layer. According to Thorpe (2005), the upper ocean comprises the sea surface, the mixed layer, and the upper part of the pycnocline. Among them, the mixed layer is crucial in controlling air-sea exchange and redistributing energy and tracers (Ferrari and Boccaletti, 2004). It is typically characterized by nearly uniform vertical profiles of temperature, salinity, and density due to active vertical mixing processes induced by the surface forcings, as shown in Figure 1.3.

Surface wind forcing can significantly contribute to ocean mixing, thus playing a dominant role in regulating upper ocean dynamics. This happens through a variety of physical mechanisms. One key mechanism is Ekman pumping, which arises from horizontal variations in wind-driven Ekman transport (Gill, 1982) and produces slow vertical motions. Wind-driven shear currents also interact with surface waves to generate Langmuir circulation, characterized by counter-rotating cells aligned with the wind direction (Craik and Leibovich, 1976). These vortices drive strong downward motions within the upper portion of the mixed layer, typically reaching 20% to 50% of its depth, and enhance vertical mixing. Under intense wind forcing, large Langmuir cells can also break down, intensifying turbulence below the surface and modifying the structure of the mixed layer.

The processes described above can significantly alter upper ocean conditions, potentially influencing the behavior of ISWs. Due to their strong nonlinearity, ISWs are highly sensitive to changes in background conditions, particularly during abrupt surface forcing events such as storms, which can rapidly alter the background velocity and stratification conditions. In the early stages of such events, the upper ocean's response is not strongly influenced by the Earth's rotation due to the short timescales involved. However, at small scales, high wind speeds still have a significant effect on the upper ocean, which can enhance near-surface turbulence through surface wave breaking, bubble injection, and foam formation at the air-sea interface (Thorpe, 2005).

These transient dynamics add complexity to the generation and propagation of ISWs. The limited understanding of ISW behavior under these conditions represents a critical knowledge gap that this thesis seeks to address.

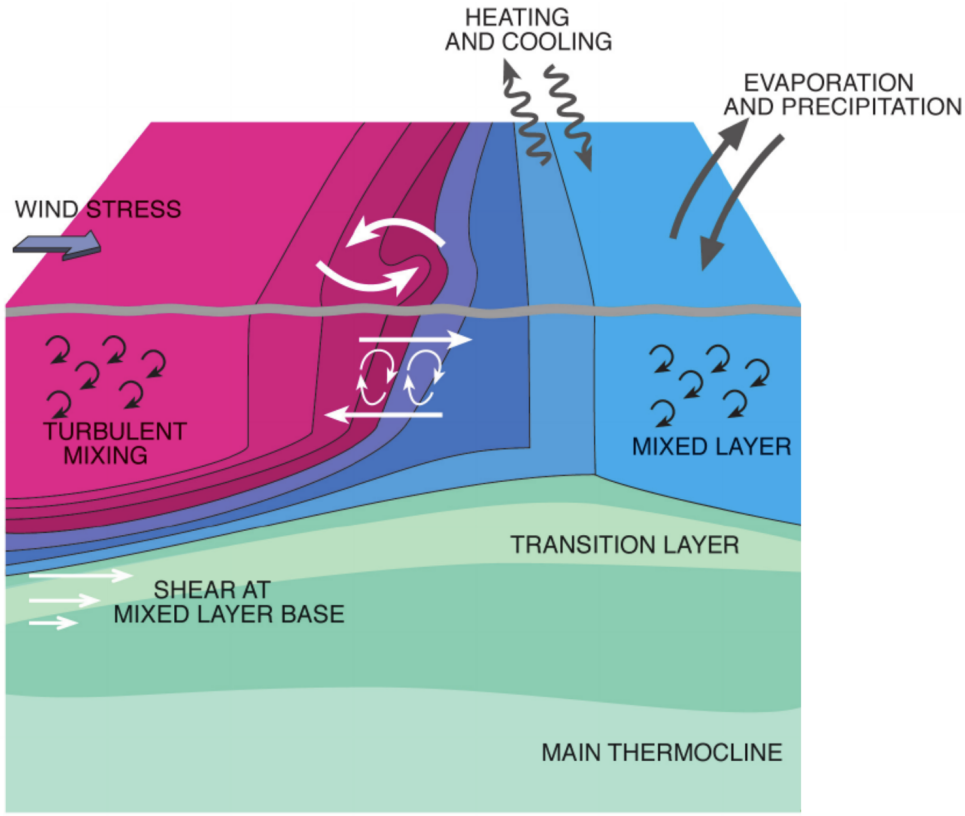


Figure 1.3: Schematic of dynamical processes in the upper ocean. Turbulent mixing induced by surface forcings maintains the mixed layer. Cited from Ferrari and Boccaletti (2004), Figure 1.

1.4 Approach to the Study of Internal Solitary Waves

ISWs have been extensively studied through a combination of observational, theoretical, and numerical approaches.

In-situ measurements, such as moored CTD profilers and ADCPs, provide time series of ISW properties at fixed locations. Repeated profiling techniques, such as yo-yo CTD casts, are also widely used to capture the rapid evolution of ISWs. While these methods can detect wave structure and variability, they are spatially limited and often fail to capture the full propagation of fast-moving ISWs.

Satellite remote sensing, including SAR and X-band radar, monitors ISWs by detecting surface roughness patterns caused by wave-induced convergence and divergence. These appear as alternating bright and dark bands (see Figure 1.4). However, satellite data capture only surface signatures and cannot directly measure subsurface features such as amplitude or wavelength. In addition, their effectiveness is reduced under adverse weather or complex sea states.

Theoretical models provide a foundational understanding of ISWs. The classical Korteweg-de Vries (KdV) theory (Benney, 1966) and its extensions (Lee and Beardsley, 1974; Helfrich and Melville, 1986; Lamb and Yan, 1996; Grimshaw et al., 2007) are widely used to describe weakly nonlinear ISW features. However, oceanic observations often reveal strongly nonlinear waveforms, motivating the use of fully nonlinear models such as the Miyata-Choi-Camassa (MCC) system (Miyata, 1985, 1988; Choi and Camassa, 1999) and the Dubreil-Jacotin-Longs (DJLs) equation (Long, 1953). The DJL model provides steady-state solutions for ISWs under arbitrary stratification and can be solved numerically. Stastna and Lamb (2002) further extended the formulation to account for background currents. Its derivation is systematically presented in Stastna (2022). A comprehensive review of these theoretical models is provided by Helfrich and Melville (2006).

Numerical simulations provide a flexible and powerful means of studying ISWs beyond the limits of observational and theoretical approaches. Nonhydrostatic ocean models such as Massachusetts Institute of Technology general circulation model (MITgcm) (Marshall et al., 1997b) and Finite Volume Community Ocean Model (FVCOM) (Qi et al., 2009) enable the simulation of internal solitary waves under realistic oceanic conditions. In this study, the MITgcm is chosen for its robust nonhydrostatic capability and various packages, which make it widely applied for small-scale internal wave processes (e.g., Dunphy and Lamb, 2014; Xie et al., 2015; Guo et al., 2021). Wind forcing is applied via the `exf` package for time-varying surface stress, and vertical turbulent mixing is parameterized using the K-Profile Parameterization (KPP). This framework allows for a realistic rep-

resentation of wind-driven upper ocean responses and their influence on internal solitary wave propagation and evolution.

1.5 Thesis Overview

This thesis investigates ISWs under varying wind conditions using a series of numerical simulations conducted with the MITgcm. The primary goal is to quantify how wind forcing influences wave characteristics such as speed, amplitude, and structure, thereby improving our understanding of how wind modulates internal wave behavior. This work contributes to a more comprehensive understanding of ISW dynamics, in which wind plays a critical role.

The remainder of this thesis is organized as follows. Chapter 2 introduces the theoretical framework, including the governing equations of fluid motion, an overview of the numerical methods used in MITgcm, and the fundamentals of the KPP mixing scheme. Chapter 3 presents a sensitivity analysis used to identify optimal numerical parameters. Chapter 4 presents the simulation results and analysis. It begins with simulations forced by constant wind stress, in which positive and negative wind stresses are applied separately. The chapter then examines the effects of two factors: wind strength and wind ramping. Chapter 5 concludes the thesis and discusses the implications, limitations, and possible directions for future work.

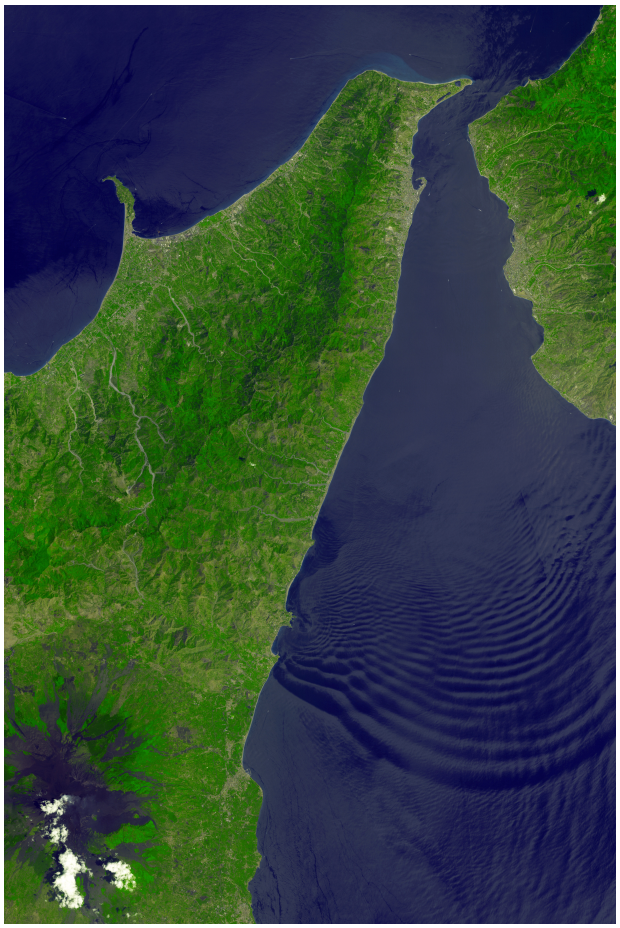


Figure 1.4: Satellite image showing internal solitary wave trains generated in the Strait of Messina and propagating southward. Alternating dark (smooth) and light (rough) surface patterns indicate the presence of ISWs. Image source: https://earthobservatory.nasa.gov/images/7630/messina-strait-italy

Chapter 2

Methods

2.1 Governing Equations

2.1.1 Basic Fluid equations under the Boussinesq Approximation

We consider an incompressible, non-rotating, stratified fluid under the Boussinesq approximation. Salinity is assumed to be constant, such that density variations arise solely from temperature. Under these assumptions, the governing equations for the fluid system are:

$$\frac{\partial \vec{u}}{\partial t} + (\vec{u} \cdot \nabla)\vec{u} = -\frac{1}{\rho_0}\nabla p - \frac{\rho}{\rho_0} g\vec{k} + \nu \nabla^2 \vec{u}, \tag{2.1}$$

$$\nabla \cdot \vec{u} = 0, \tag{2.2}$$

$$\frac{\partial T}{\partial t} + (\vec{u} \cdot \nabla)T = \kappa \nabla^2 T, \tag{2.3}$$

$$\rho = \rho(T), \tag{2.4}$$

In these equations, the coordinates x, y, and z represent the eastward, northward, and upward directions, respectively. The velocity vector $\vec{u} = u\vec{i} + v\vec{j} + w\vec{k}$ consists of the streamwise (u), spanwise (v), and vertical (w) components, with the unit vectors $\vec{i}$, $\vec{j}$, and $\vec{k}$ corresponding to the x, y, and z axes. The gradient operator is expressed as $\nabla = \frac{\partial}{\partial x}\vec{i} + \frac{\partial}{\partial y}\vec{j} + \frac{\partial}{\partial z}\vec{k}$, and the Laplacian operator $\nabla^2 = \frac{\partial^2}{\partial x^2} + \frac{\partial^2}{\partial y^2} + \frac{\partial^2}{\partial z^2}$. The parameters ρ and ρ_0 represent the fluid density and reference density under the Boussinesq approximation. p is the pressure, g is gravitational acceleration, and T denotes temperature. ν and κ represent molecular viscosity and diffusivity, respectively.

The Boussinesq approximation is applied by replacing ρ with a reference density ρ_0 in the fluid equations, except in the buoyancy term in the momentum equations (Eq. 2.1) and the equation of state (Eq. 2.4). This approximation is built on the assumption that fluid compressibility is negligible. Several requirements must therefore be satisfied. First, the Mach number must satisfy $Ma = U/c_s \ll 1$, where U is the flow speed and c_s is the sound speed. Density variations caused by pressure changes become significant at finite or large Mach numbers, such that $\nabla \cdot \mathbf{u}$ can no longer be neglected. Second, the vertical scale of the flow L should satisfy $L \ll c_s^2/g$; otherwise, hydrostatic pressure variations can cause significant changes in density. When compressibility effects are small, the Boussinesq approximation applies when the relative density

$$\frac{\rho'}{\rho} = O(10^{-3}) \ll 1,$$

is sufficiently small in the ocean, where $\rho' = \rho - \rho_0$. Thus, in the full form of the momentum equation,

$$\left(1 + \frac{\rho'}{\rho_0}\right) \frac{D\vec{u}}{Dt} = -\frac{1}{\rho_0}\nabla p - \frac{\rho}{\rho_0} g\vec{k} + \nu\nabla^2\vec{u}, \tag{2.5}$$

the contribution of the term ρ'/ρ_0 to the inertia term can be neglected. The small relative density variation also ensures that the density variation term $\frac{1}{\rho}\frac{D\rho}{Dt}$ in the full form of the continuity equation is negligible compared to the velocity divergence term $\nabla \cdot \vec{u}$. Therefore, the continuity equation is written in the incompressible form (Eq. 2.2).

Different from the standard Navier-Stokes equation system, where the primary variables are the velocity field $\vec{u}$ and density ρ, Eqs. 2.1-2.4 do not include an evolution equation for density. Instead, density is determined through the temperature equation, Eq. 2.3, and the equation of state, Eq. 2.4. Physically, this reflects the fact that seawater density depends on temperature, salinity, and pressure, described as

$$\rho = \rho(T, S, P). \tag{2.6}$$

Therefore, density is treated as a diagnostic variable in the equations of seawater motion. Since salinity variations and seawater compressibility are neglected in this study, density can be approximated as a function of temperature.

2.1.2 MITgcm governing equations

For this thesis, the governing equations solved by the non-hydrostatic version of MITgcm are given by Eqs. 2.7–2.10 and are solved numerically to simulate fluid motion under

external wind forcing.

$$\frac{\partial \vec{u}}{\partial t} + (\vec{u} \cdot \nabla)\vec{u} = -\frac{1}{\rho_0}\nabla p - \frac{\rho}{\rho_0} g\vec{k} + \nabla_H \cdot (\nu_H \nabla_H \vec{u}) + \frac{\partial}{\partial z}\left(\nu_V \frac{\partial \vec{u}}{\partial z}\right) + F_{\text{wind}}(z)\vec{i}, \tag{2.7}$$

$$\nabla \cdot \vec{u} = 0, \tag{2.8}$$

$$\frac{\partial T}{\partial t} + (\vec{u} \cdot \nabla)T = \nabla_H \cdot (\kappa_H \nabla_H T) + \frac{\partial}{\partial z}\left(\kappa_V \frac{\partial T}{\partial z}\right), \tag{2.9}$$

$$\rho(T) = \rho_0 \left[1 - \alpha(T - T_0)\right], \tag{2.10}$$

where $\vec{u}$ is the velocity vector, ρ_0 is the reference density and ρ is density, p is pressure, g is gravitational acceleration. The horizontal gradient operator $\nabla_H = \frac{\partial}{\partial x}\vec{i} + \frac{\partial}{\partial y}\vec{j}$. ν_H and ν_V are the horizontal and vertical eddy viscosity coefficients. κ_H and κ_V are the horizontal and vertical eddy diffusivity coefficients.

$F_{\text{wind}}(z)$ in Eq. 2.7 is the external wind stress term applied to the ocean surface. In the MITgcm, the forcing term is defined as:

$$F_{\text{wind}}(z) = \begin{cases} \frac{\tau_{\text{wind}}}{\rho_0 \Delta z(1)}, & \text{if } z = z_c(1), \\ 0, & \text{if } z < z_c(1), \end{cases}$$

where τ_{wind} is the surface wind stress, measured in N/m^2. It represents the force exerted per unit area, and $\Delta z(1)$ denotes the height of the surface grid cell. $z_c(1)$ denotes the centre of the first vertical grid cell counted from the surface, where the wind stress is applied.

$F_{\text{wind}}(z)$ describes the body force applied to a unit mass of fluid. In the model, wind stress is only applied at the top layer and propagates downward through eddy viscous stress between vertically adjacent grid cells, as illustrated in Figure 2.1.

Eq. 2.10 is the linear equation of state, which is an empirical evaluation, obtained by applying a first-order Taylor expansion about a reference temperature T_0. According to McWilliams (2006), the thermal expansion coefficient for seawater is typically $\alpha = 2 \times 10^{-4}\ \text{K}^{-1}$, which is also the value adopted in the present study.

2.1.3 Dimensionless Numbers

In the application of MITgcm, the Richardson number Ri is used. Shear instability is induced by velocity shear in fluids, while it can be suppressed by stratification. Therefore, the dimensionless number Ri quantifies flow stability by comparing the relative importance

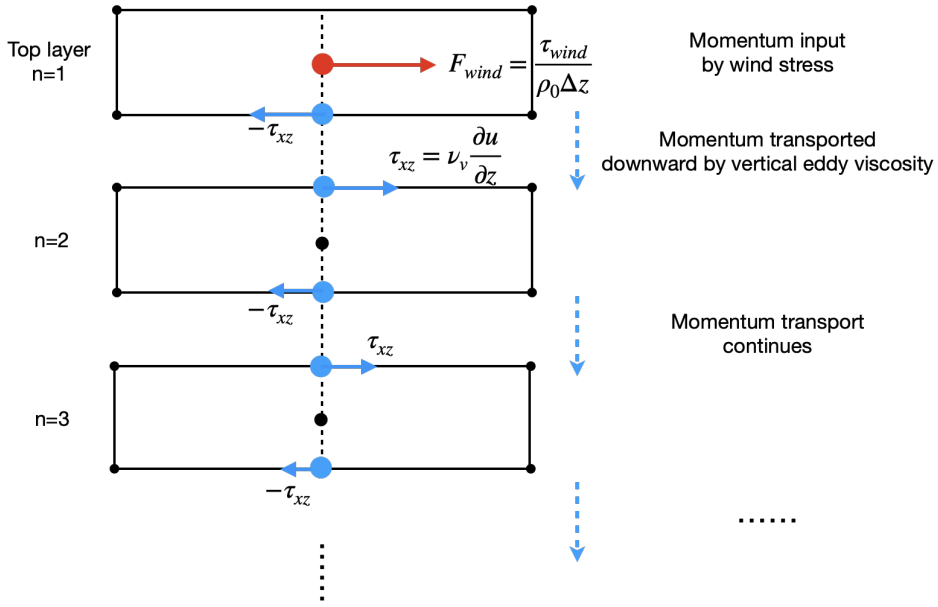


Figure 2.1: Downward propagation of momentum from wind. F_{wind} represents wind force acting only on the surface layer. τ_{xz} denotes eddy viscous shear stress that transfers the wind-induced momentum downward. Only the first three grid layers are shown.

of buoyancy to shear. Ri has a few expressions, including the gradient Richardson number Ri_g, the bulk Richardson number Ri_b, and the flux Richardson number Ri_f. The first two are used in this study and introduced here.

The gradient Richardson number, Ri_g, is calculated as the ratio of local stratification strength to shear strength, both expressed in gradient form. It can be used to evaluate local shear instability and is defined as

$$Ri_g = \frac{\alpha g \dfrac{\partial T}{\partial z}}{\left(\dfrac{\partial U}{\partial z}\right)^2 + \left(\dfrac{\partial V}{\partial z}\right)^2}. \tag{2.11}$$

Linear theory states that, for inviscid parallel flow, $Ri_g < 0.25$ is a necessary condition for shear instability to occur. Negative values of Ri_g correspond to unstable stratification and indicate the possibility of convective instability.

The bulk Richardson number Ri_b is an approximation of Ri_g that evaluates the stability of a fluid layer with thickness Δz. It is expressed as

$$Ri_b = \frac{\alpha g \, \Delta T \, \Delta z}{(\Delta U)^2 + (\Delta V)^2}. \tag{2.12}$$

As Δz approaches zero, Ri_b approaches Ri_g. Although the critical threshold of 0.25 for shear instability does not strictly apply to Ri_b, small values of Ri_b generally indicate that shear is strong relative to stratification and that the fluid layer may be susceptible to shear instability.

2.2 Numerical Implementation in the MITgcm Model

The governing equations described in Section 2.1.2 are solved numerically using the MITgcm. This section summarizes the numerical implementation adopted in this study, including the general solution procedure, the temporal schemes used for different terms, and the spatial discretization based on the Finite Volume Method (FVM).

2.2.1 Overview of the Numerical Procedure

This study uses a two-dimensional nonhydrostatic configuration of the MITgcm in the (x, z) domain, with a linear equation for the free-surface. Under this configuration, the

Table 2.1: Summary of temporal treatments used in the model configuration.

Model term	**Temporal scheme**
Momentum advection	Explicit
Horizontal viscosity	Explicit
Vertical viscosity	Implicit
Horizontal temperature diffusion	Explicit
Vertical temperature diffusion	Implicit
External momentum forcing	Explicit
Free surface	Crank-Nicolson
Surface pressure gradient	Crank-Nicolson
Barotropic flow divergence	Crank-Nicolson

pressure potential can be decomposed as

$$\phi(x,z,t) = \phi_s(x,t) + \phi_{\text{hyd}}(x,z,t) + \phi_{\text{nh}}(x,z,t), \tag{2.13}$$

where ϕ_s represents the barotropic pressure potential associated with the free-surface displacement, ϕ_{hyd} is the hydrostatic pressure potential associated with density variations, and ϕ_{nh} is the nonhydrostatic pressure potential.

The FVM model implements a predictor-corrector numerical procedure, as introduced in Marshall et al. (1997b). In each time step, explicitly treated tendencies are first used to form an intermediate velocity field. The barotropic pressure contribution is then applied to satisfy the depth-integrated continuity constraint associated with the free surface. The nonhydrostatic pressure potential is subsequently obtained from an elliptic equation and used to further update the velocity field. After these updates, the velocity field satisfies the local incompressibility constraint given in Eq. 2.8.

2.2.2 Temporal Scheme

The MITgcm allows explicit and implicit temporal schemes to be combined. The schemes used in this study are summarized in Table 2.1. Explicit terms in the momentum and tracer equations are advanced using the second-order Adams-Bashforth scheme. Tendency is defined as the local rate of change of a vector or scalar quantity with time at a given point in space (American Meteorological Society, 2026). For a generic tendency G, the extrapolated tendency at the half-time level is written as

$$G^{(n+1/2)} = \left(\frac{3}{2} + \epsilon\right) G^n - \left(\frac{1}{2} + \epsilon\right) G^{n-1}, \tag{2.14}$$

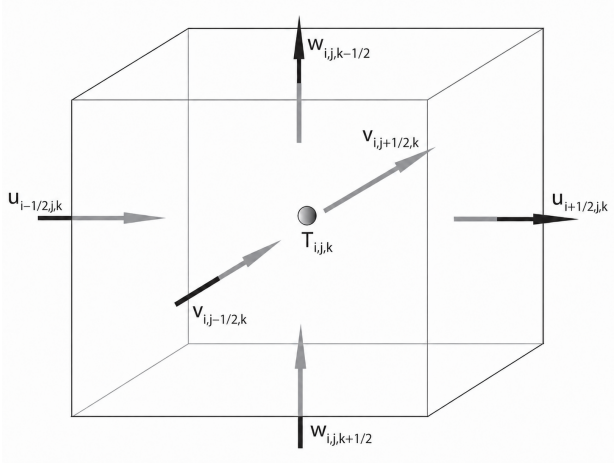


Figure 2.2: Finite-volume discretization on an Arakawa C grid. Tracer variables are located at cell centres, while velocity components are located at cell faces, where the arrows indicate the corresponding flux directions. Adapted from Gelderloos et al. (2016) Fig. 1, following the MITgcm indexing convention.

where ϵ is a stabilization parameter. In this study, $\epsilon = 0.1$ is used to reduce weak numerical instabilities associated with oscillatory modes, as suggested by Marshall et al. (1997a).

Terms treated with the Crank-Nicolson scheme are evaluated using a weighted average of the old and new time levels:

$$\gamma\eta^{n+1} + (1-\gamma)\eta^{n}, \qquad \gamma = \frac{1}{2}. \tag{2.15}$$

For the linear free-surface gravity-wave system, applying the Crank–Nicolson scheme to the surface pressure gradient and the divergence of the barotropic flow yields a neutrally stable temporal scheme (Campin et al., 2004).

Vertical viscosity and diffusion terms are treated implicitly because the KPP scheme can generate large vertical diffusivity values for both momentum and temperature. If these terms were treated explicitly instead, the resulting diffusive stability constraint would require very small time steps (Press et al., 1986).

2.2.3 Spatial Scheme

The spatial discretization is based on the FVM (Figure 2.2). In this method, the partial differential equations are integrated over each control volume, which corresponds to a com-

putational cell. By the divergence theorem, divergence terms in the governing equations are converted into surface flux integrals. Therefore, the change of a quantity within a cell is balanced by the net flux through the cell boundaries. Since the flux leaving one cell enters the neighboring cell through the same face, the finite-volume formulation guarantees local conservation.

On the Arakawa C grid (Arakawa and Lamb, 1977), velocity components are located at the centres of the cell faces through which their corresponding fluxes pass, whereas tracer variables are located at cell centres. The advantages of the Arakawa C grid in the model are discussed by Marshall et al. (1997a). In this study, both momentum and temperature advection are discretized using second-order centred schemes.

For the second-order centred temperature advection scheme, temperature values are interpolated from cell centres to cell faces. For a generic tracer ψ, the value at the cell face indexed by $i + 1/2$ is approximated as

$$\psi_{i+1/2,k} = \frac{1}{2}\left(\psi_{i,k} + \psi_{i+1,k}\right). \tag{2.16}$$

The corresponding tracer flux across the face is then

$$F_{x,i+1/2,k} = U_{i+1/2,k}\psi_{i+1/2,k} = U_{i+1/2,k}\frac{\psi_{i,k} + \psi_{i+1,k}}{2}, \tag{2.17}$$

where $U_{i+1/2,k}$ is the volume flux through the corresponding cell face. The same centred approximation is applied to the vertical advective flux. The scheme is second-order accurate for smooth solutions.

2.3 Turbulence Closure and Vertical Mixing

2.3.1 Reynolds decomposition and closure problem

In geophysical flows, the spatial and temporal scales of the geophysical characteristics are much larger than those of the turbulence involved. This means that resolving the fluid equations to account for small-scale turbulence and large-scale geophysical characteristics simultaneously is challenging due to computational limitations. It is therefore appropriate to introduce the Reynolds decomposition method, in which the variables are decomposed into mean and turbulent components:

$$u = U + u', \quad \overline{U} = U, \quad \overline{u'} = 0,$$

where U represents the mean flow, u' represents the turbulent fluctuation and the overbar $\overline{\cdot}$ denotes the averaging operation.

This decomposition generates the Reynolds-Averaged Navier-Stokes (RANS) equations; however, it also introduces the closure problem. This can be illustrated using a simplified fluid equation, the Burgers equation:

$$u_t + uu_x = \nu u_{xx}, \tag{2.18}$$

where u is the velocity and ν is the kinematic viscosity. Applying the Reynolds decomposition, Eq. 2.18 transforms into

$$U_t + UU_x = \nu U_{xx} - \frac{1}{2}\frac{\partial}{\partial x}\overline{u'u'}, \tag{2.19}$$

where the unknown term $\overline{u'u'}$ prevents the equation from being solved directly. This illustrates the core idea of the closure problem.

In the full set of fluid equations, Reynolds averaging introduces the Reynolds stress tensor, defined as

$$\tau_{ij} = -\rho_0 \overline{u_i' u_j'},$$

which represents the transport of momentum caused by turbulent velocity fluctuations. The frictional force per unit volume is defined as the divergence of the Reynolds stress tensor:

$$F_i^R = \frac{\partial \tau_{ij}}{\partial x_j} = \rho_0 \frac{\partial \overline{u_i' u_j'}}{\partial x_j}. \tag{2.20}$$

Since τ_{ij} cannot be determined directly from the resolved mean-flow variables, a turbulence closure model is required.

2.3.2 Representation of turbulent processes in the MITgcm

The Boussinesq eddy viscosity assumption states that τ_{ij} can be written as

$$\tau_{ij} = \rho_0 \nu \left(\frac{\partial \overline{u}_i}{\partial x_j} + \frac{\partial \overline{u}_j}{\partial x_i} \right) - \frac{2}{3}\rho_0 k \delta_{ij}, \tag{2.21}$$

where $k = \frac{1}{2}\langle u_i' u_i' \rangle$ is the turbulent kinetic energy (TKE), and ν is the eddy viscosity.

In contrast, the Reynolds stress in the MITgcm is given by

$$\tau_{xz} = \tau_{zx} = \rho_0 \nu_V \frac{\partial u}{\partial z} + \rho_0 \nu_H \frac{\partial w}{\partial x}, \tag{2.22}$$

$$\tau_{yz} = \tau_{zy} = \rho_0 \nu_V \frac{\partial v}{\partial z} + \rho_0 \nu_H \frac{\partial w}{\partial y}, \tag{2.23}$$

$$\tau_{xy} = \tau_{yx} = \rho_0 \nu_H \left(\frac{\partial u}{\partial y} + \frac{\partial v}{\partial x} \right), \tag{2.24}$$

$$\tau_{xx} = 2\rho_0 \nu_H \frac{\partial u}{\partial x}, \quad \tau_{yy} = 2\rho_0 \nu_H \frac{\partial v}{\partial y}, \quad \tau_{zz} = 2\rho_0 \nu_V \frac{\partial w}{\partial z}. \tag{2.25}$$

Based on Eq. 2.20, the viscous friction force in Eq. 2.7 can be obtained as

$$\rho_0 \left(\nu_H \Delta + \nu_V \partial_z^2 \right) \vec{u}, \qquad \Delta \equiv \partial_x^2 + \partial_y^2,$$

where ν_H and ν_V are the horizontal and vertical eddy viscosities, respectively.

Compared to the Boussinesq eddy viscosity assumption, MITgcm represents vertical and horizontal eddy processes separately by introducing ν_V and ν_H. In stratified fluids, horizontal and vertical motions occur over distinct spatial and temporal scales; therefore, turbulent motions usually have different strengths in the horizontal and vertical directions. As a result, uniform eddy diffusion coefficients cannot adequately capture the distinct dynamics in the two directions. The use of separate horizontal and vertical eddy diffusion coefficients is a conventional approach to turbulence parameterization in ocean models.

However, as Miles (1994) points out, constructing the Reynolds stress tensor in this way causes τ_{ij} to depend on fluid rotation rather than solely on deformation. For example, when $\nu_V \neq \nu_H$, τ_{xz} is a linear combination of the deformation $(\partial u/\partial z + \partial w/\partial x)$ and the rotation $(\partial u/\partial z - \partial w/\partial x)$. Physically, this is incorrect because the parameterized turbulent stress should be independent of the fluid parcel's rotation. Mathematically, it violates the objectivity requirement for a constitutive equation; in other words, the Reynolds stress erroneously depends on rigid-body rotation of the reference frame. An objective anisotropic eddy-viscosity formulation should instead express the Reynolds stress solely in terms of the symmetric strain rate tensor.

Another limitation is that, compared with the Boussinesq eddy viscosity assumption, which parameterizes only the deviatoric components of the stress tensor, τ_{ij} in the MITgcm does not separate the isotropic component from the stress tensor. As a result, this formulation cannot provide a reasonable TKE, which is derived as

$$\frac{1}{2}\rho_0 \langle u_k' u_k' \rangle = -\frac{1}{2}\rho_0 \tau_{kk} = -\rho_0 \nu_k \partial_k u_k = \rho_0 \left(\nu_H - \nu_V \right) \partial_z w. \tag{2.26}$$

When $\nu_H < \nu_V$ and $\partial_z w > 0$, the TKE becomes negative; when $\nu_H = \nu_V$, it reduces to zero. Since TKE in turbulent processes must always remain positive, this parameterization clearly fails to represent TKE accurately.

Thus, while the anisotropic eddy-viscosity model used in the MITgcm, as well as in other ocean models, is a conventional and practical approach for representing turbulence in ocean models, it is not fully rigorous and should be applied with caution.

2.4 Vertical Mixing Scheme: K-Profile Parameterization

2.4.1 General Introduction

The KPP is a widely used vertical mixing scheme in global and regional ocean models, such as MITgcm, Regional Ocean Modeling System (ROMS), and HYbrid Coordinate Ocean Model (HYCOM). Originally proposed by Troen and Mahrt (1986) to parameterize atmospheric turbulence, it was later adapted to ocean boundary layers by Large et al. (1994). KPP provides a physics-based representation of turbulent mixing by including both local and nonlocal transport. Local transport is caused by gradients; i.e., momentum or concentration is transported downgradient. Related physical processes in the ocean include, for example, wind-induced shear currents and upper-ocean restratification driven by surface heating. Nonlocal transport is driven by convection, which is associated with unstable density structures. Examples of nonlocal transport include surface cooling and precipitation. KPP explicitly considers both local and nonlocal transport, making it applicable across a wide range of atmospheric conditions.

The schematic of an ocean profile is presented in Figure 2.3. In the ocean surface boundary layer (OSBL), the motion of seawater is strongly affected by atmospheric forcing, such as wind stress, surface heat flux, and radiation, which generates active turbulence. In the region below the OSBL, turbulence is generated by interior instabilities, such as internal wave breaking and shear instabilities associated with flow over topography. Given the distinct physical processes governing mixing in these two regions, KPP first determines the boundary layer depth and then parameterizes the eddy diffusivities separately within the boundary layer and the ocean interior.

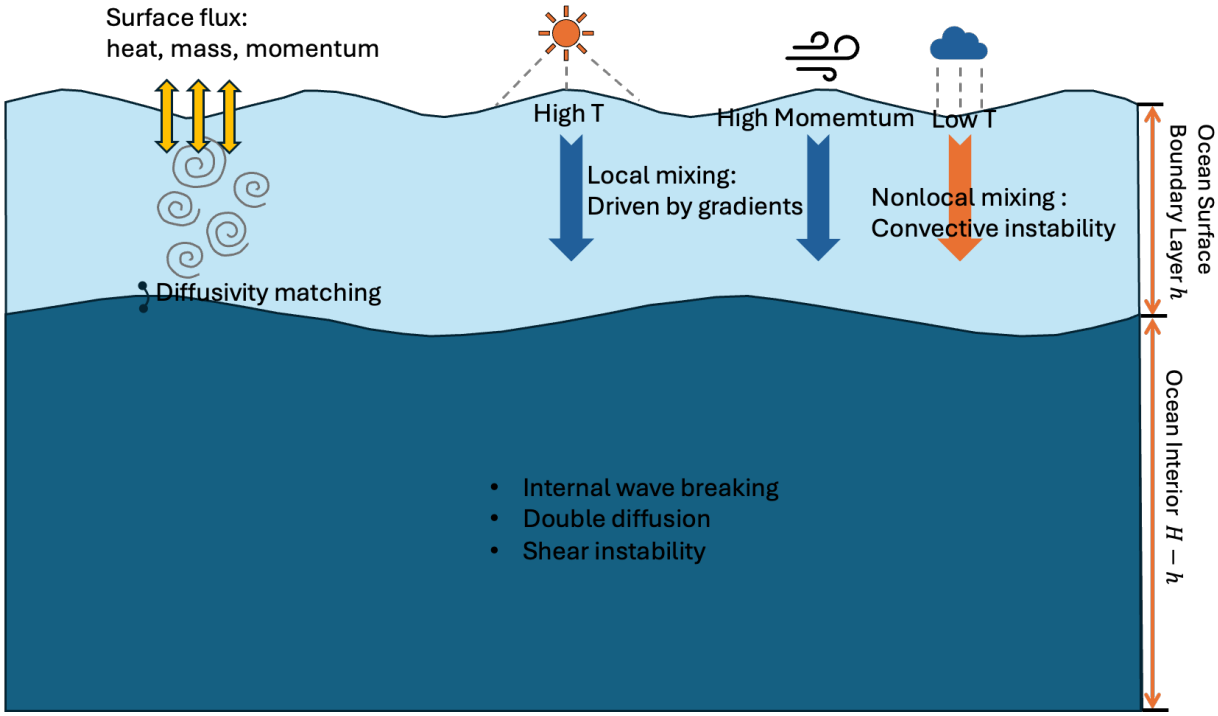


Figure 2.3: Diagram of ocean profiles associated with the KPP boundary layer parameterization. The ocean has a total depth $H + \eta$, where η is the height of the free surface. The ocean surface is subject to external fluxes, driving turbulence within the ocean surface boundary layer (OSBL) to a depth of h. Below the OSBL is the ocean interior, where turbulence is considered to be dominated by processes including internal wave breaking, double diffusion, and shear instability. The eddy diffusivities in the OSBL and ocean interior are matched at the base of the OSBL ($z = -h$).

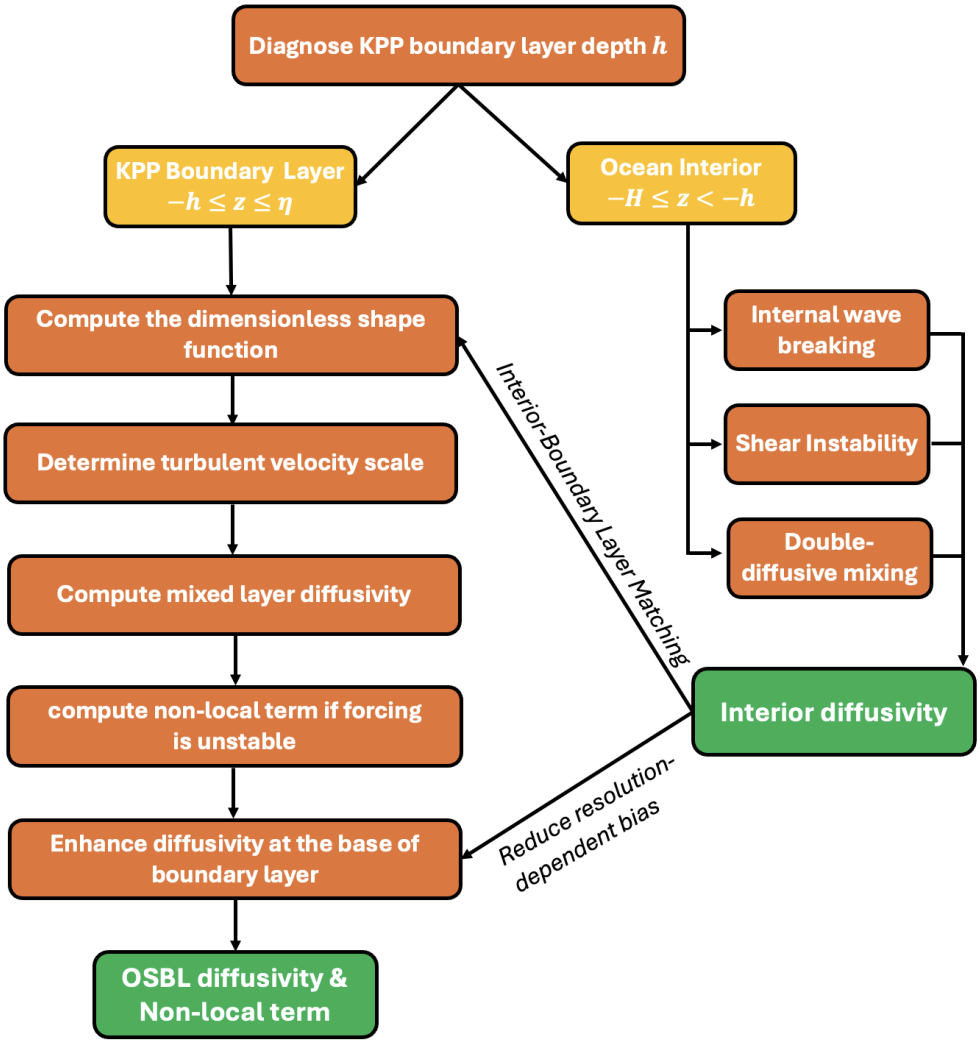


Figure 2.4: Procedure for calculating the KPP diffusivity and nonlocal transport terms in the KPP scheme. The interior diffusivity is computed first and used as a reference to ensure smooth matching of the boundary-layer diffusivity at the interface.

2.4.2 General Structure of KPP Scheme

For fluids with a free surface, the vertical coordinate z extends from the ocean bottom (z=-H) to the free-surface height, $z = \eta$. The detailed procedure for calculating the KPP diffusivity K_ψ and nonlocal transport term γ_ψ is shown in Figure 2.4. The detailed formulation is provided in this section.

Determine the Boundary Layer Depth

The boundary layer depth h is defined using the bulk Richardson number Ri_b (Eq. 2.12). In KPP, Ri_b is modified by introducing the unresolved velocity shear V_t, and is expressed as

$$Ri_b(z) = \frac{(b_{sl} - b(z))z}{|u_{sl} - u(z)|^2 + V_t^2(z)}. \tag{2.27}$$

The depth h is determined by locating the depth at which $Ri_b(h)$ is equal to a critical value Ri_c which is traditionally set to 0.3. Here, b_{sl} and u_{sl} are the buoyancy and horizontal velocity averaged over the surface layer, respectively. The unresolved shear term, $V_t^2(h)$, is estimated as

$$V_t^2(h) = \frac{\sqrt{0.2}C_v}{Ri_c\kappa^{2/3}}(c_s\epsilon)^{-1/6}hN_e w_* \tag{2.28}$$

where C_v is a constant related to the ratio of interior to entrainment depth, $\kappa = 0.4$ is the von Kármán constant, N_e represents the stratification in the entrainment layer, and w_* is the convective velocity scale, determined by:

$$w_* = (-h\overline{(w'b')}_{sfc})^{1/3} \tag{2.29}$$

where $(w'b')_{sfc}$ represents the surface turbulent buoyancy flux.

The Ocean Interior

In the ocean interior ($-H \leq z < -h$), the subgrid turbulent vertical flux of scalar ψ is given by

$$\overline{(w'\psi')} = -K_\psi \frac{\partial \psi}{\partial z} \tag{2.30}$$

where ψ represents resolved quantities such as u, v, w, T, S, and ψ' represents the unresolved turbulent terms.

Turbulent mixing in the ocean interior is driven by the combined effects of shear instability, internal wave breaking, and double diffusion. Since salinity is assumed to be constant in this study, double diffusion will not be included, and only the first two processes are parameterized. The total interior diffusivity is represented as

$$K_\psi = K_\psi^s + K_\psi^w \tag{2.31}$$

where K_ψ^s accounts for mixing due to resolved shear instability, and K_ψ^w represents mixing driven by internal wave breaking.

The susceptibility for shear instability to occur is characterized by the gradient Richardson number, Ri_g. In the KPP scheme, $Ri_0 = 0.7$ is used as the critical gradient Richardson number. This value is much larger than the theoretical critical value 0.25 because limitations in grid resolution can underestimate velocity shear, thereby producing larger values of Ri_g.

The diffusivity induced by shear instability, K_ψ^s, is parameterized as:

$$K_\psi^s = \begin{cases} \nu_0 & Ri_g < 0 \\ \left[1 - \left(\frac{Ri_g}{Ri_0}\right)^2\right]^P \nu_0 & 0 < Ri_g < Ri_0 \\ 0 & Ri_g > Ri_0 \end{cases}$$

where $\nu_0 = 50 \times 10^{-4}\,\mathrm{m^2 s^{-1}}$ and $P = 3$.

For the diffusivity induced by internal wave breaking, Large et al. (1994) suggested that the momentum diffusivity K_m^w and scalar diffusivity K_s^w should be:

$$K_s^w = 0.1 \times 10^{-4}\,\mathrm{m^2 s^{-1}}$$
$$K_m^w = 1.0 \times 10^{-4}\,\mathrm{m^2 s^{-1}}$$

The Ocean Surface Boundary Layer

The turbulence in OSBL ($-h \le z \le \eta$) is considered to be driven by the surface forcing. To parameterize the turbulent processes in this region, a non-dimensional parameter σ is introduced to represent the relative position within the OSBL:

$$\sigma = \frac{-z + \eta}{h}, \quad 0 \le \sigma \le 1 \tag{2.32}$$

The subgrid turbulent vertical flux of any scalar or vector quantity ψ in the OSBL is parameterized as

$$\overline{(w'\psi')} = -K_\psi \frac{\partial \psi}{\partial z} + K_\psi \gamma_\psi. \tag{2.33}$$

Compared with Eq. 2.30, the introduction of the nonlocal term γ_ψ allows the nonlocal turbulent flux, $K_\psi \gamma_\psi$, associated with convective instabilities to be represented.

The eddy diffusivity K_ψ is given by

$$K_\psi(\sigma) = h w_\psi(\sigma) G(\sigma) \tag{2.34}$$

where h is the KPP boundary layer depth, w_ψ is the turbulent velocity scale, and $G(\sigma)$ is the vertical shape function. Solving for K_ψ requires determining these three terms in Eq.2.34.

The first term is the boundary layer depth h, determined using Eq. 2.27. In the OSBL, the magnitude of K_ψ at a given nondimensional depth is proportional to h. Therefore, in the KPP scheme, a deeper boundary layer also indicates stronger eddy viscosity and diffusivity.

The second term, the turbulent velocity scale w_ψ, is given by Eqs. 2.35-2.36, which are derived by extending Monin–Obukhov similarity theory from the surface layer to the entire KPP boundary layer.

$$w_\psi(\sigma) = \frac{\kappa u^*}{\phi_\psi(\sigma h/L)}, \quad 0 < \sigma < \epsilon \tag{2.35}$$

$$w_\psi(\sigma) = \frac{\kappa u^*}{\phi_\psi(\epsilon h/L)}, \quad \epsilon < \sigma < 1 \tag{2.36}$$

where u^* is the friction velocity, ϵ defines the thickness of the surface layer, and ϕ_ψ is the non-dimensional flux profile.

The third term, the vertical shape function $G(\sigma)$, is given by a third-order polynomial

$$G(\sigma) = a_0 + a_1\sigma + a_2\sigma^2 + a_3\sigma^3. \tag{2.37}$$

$G(\sigma)$ characterizes the vertical structure of turbulent diffusivity and nonlocal flux. The coefficients a_0, a_1, a_2, a_3 are determined by surface boundary conditions and the continuity requirement at the base of the KPP boundary layer ($z = -h$). This ensures that the turbulent flux in the OSBL is smoothly transmitted into the ocean interior.

The nonlocal term γ_ψ in Eq. 2.33, which represents turbulent flux due to convective instability, is non-zero for tracers under unstable surface buoyancy forcing. It is given by

$$\gamma_\psi = C_* \kappa (c_s \kappa \epsilon)^{1/3} \left(\frac{\overline{(w'\psi')_{sfc}}}{w_\psi h} \right) \tag{2.38}$$

where κ is the von Kármán constant, and c_s and C_* are constants. The term $(w'\psi')_{sfc}$ represents the vertical turbulent flux at the ocean surface due to air-sea interactions.

Chapter 3

Sensitivity Analysis

To effectively use the MITgcm model to study the role of wind in internal wave evolution, it is essential to select optimal model parameters. This chapter presents sensitivity tests conducted to determine the best grid resolutions, mixing closure schemes, and diffusion parameters.

3.1 Model Configuration and Initial Fields

The 2-D simulations are conducted in the x-z plane, representing a simplified configuration with $\partial/\partial y = 0$ and no rotation. The computational domain extends $L = 15$ km horizontally and has a total water depth of $H = 600$ m. A flat bottom is used in all experiments. Boundary conditions consist of periodic boundaries on the sides, an implicit free surface condition at the upper boundary, and a free-slip condition at the bottom. The wind stress is prescribed as $\tau_{\text{wind}} = 0.3\ \text{N}\,\text{m}^{-2}$, and applied on the upper boundary.

The background density field is defined by an exponential density profile, given by

$$\overline{\rho}(z) = \rho_2 - (\rho_2 - \rho_1) \exp\left(\frac{z}{d_p}\right) \tag{3.1}$$

where $\rho_1 = 1022\ \text{kg/m}^3$ and $\rho_2 = 1027\ \text{kg/m}^3$ are the densities at the surface and bottom, respectively, and $d_p = 50$ m represents the scale of the pycnocline's thickness. By specifying the density profile $\overline{\rho}(z)$, the corresponding temperature profiles are computed from the equation of state (Eq. 2.10) with $\alpha = 2 \times 10^{-4}\,\text{K}^{-1}$ and used as the initial fields. This setup means that there is no mixed layer in the initial state.

The background velocity field is zero in the initial state. Therefore, each simulation is initialized with a mode-1 ISW centred at $x = 1.5$ km under the prescribed stratification conditions. The initial amplitude of the ISWs is set to $A_0 = -58$ m. The initial ISW field is computed by numerically solving the DJL equation, which describes a steady and inviscid internal solitary wave propagating with no forcing.

$$\nabla^2\eta + \frac{N^2(z-\eta)}{c^2}\eta = 0, \tag{3.2}$$

where η is the isopycnal displacement from its far-upstream value, N^2 is the buoyancy frequency, and c is the propagation speed of the ISW. The numerical solution is obtained using the DJLes solver (Dunphy et al., 2011). The solver applies the Fast Fourier Transform method to solve the equation numerically, imposing periodic boundary conditions at the sides.

To evaluate the model's sensitivity to the vertical mixing closure, grid resolution, and background diffusive parameters, 17 simulations are performed, as listed in Table 3.1. Here, Δx and Δz denote the horizontal resolution and the vertical resolution in the upper 300 m, respectively. The full grid configurations are provided in Table 3.2. Non-uniform grids are used because, below $z = -300$ m, the density profile is nearly uniform and the amplitude of internal solitary waves approaches zero. Therefore, coarser vertical grids are employed in this deep region to improve computational efficiency. The Prandtl number, $Pr = \nu/\kappa$, is fixed at 1, such that $\nu_h = \kappa_h$ and $\nu_v = \kappa_v$. Thus, A_h and A_v serve as generalized diffusive parameters that represent the background horizontal and vertical viscosities and diffusivities, respectively.

3.2 Sensitivity Tests

The sensitivity experiments are organized into six groups to facilitate comparison, as illustrated in both Figure 3.1 and detailed in Table 3.1. These experiments are used to assess the effects of the vertical mixing closure, grid resolution, and background diffusive parameters on the simulation results and to identify the optimal parameter settings for the main simulations.

3.2.1 KPP Turbulent Parameterization

The influence of a vertical mixing parameterization is evaluated by comparing results from Groups 1, 2, and 3.

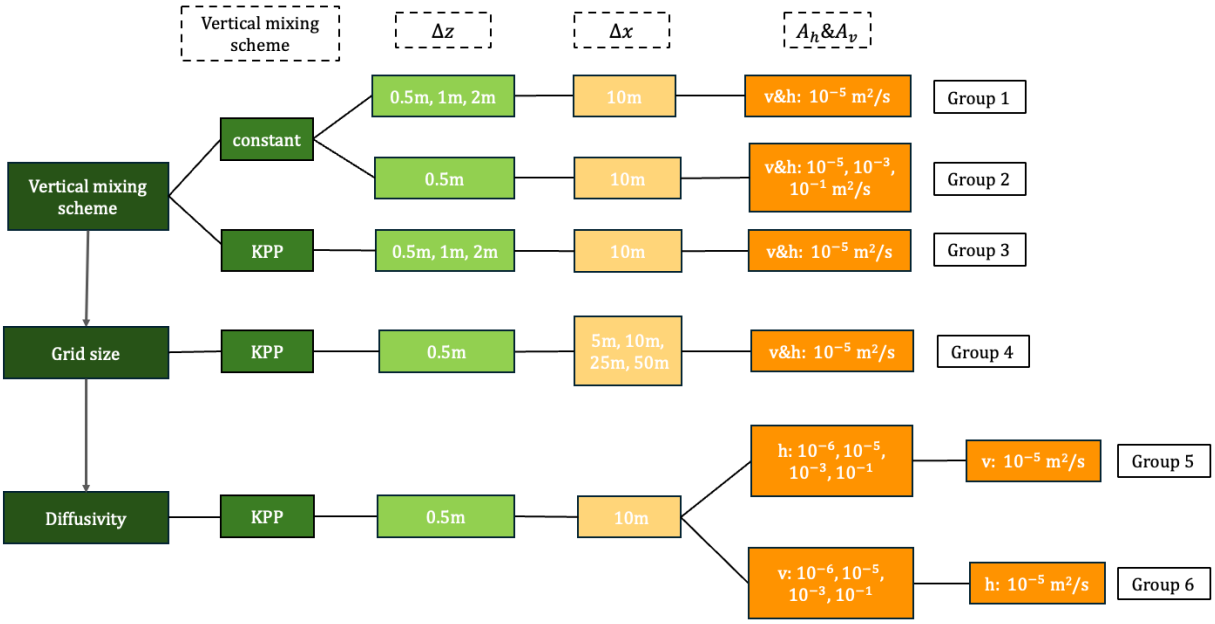


Figure 3.1: Experimental design for the sensitivity tests. The vertical mixing scheme uses either constant eddy diffusivity parameters (denoted as "constant") or KPP. Δx and Δz denote the horizontal and vertical grid sizes, respectively. A_h and A_v denote the horizontal and vertical eddy viscosity/diffusivity, respectively.

In Group 1 (cases C1-C3), a constant diffusivity is applied for different vertical grid sizes. Figure 3.2 presents the results at $t = 0.7\,\mathrm{h}$, when the wave begins to reshape. Panels (a)-(c) show the simulation results, and panel (d) presents the corresponding vertical profiles of the wind-induced background current, $U_0(z)$.

From case C1 to case C3, Δz increases. The three simulations exhibit several similarities. First, the wind-driven momentum remains concentrated near the surface. Second, the waves undergo strong instabilities and substantial deformation, particularly near the surface. However, the simulation results are dependent on the vertical grid size. The profiles of $U_0(z)$ indicate that increasing Δz leads to lower peak surface velocities and a more gradual decay with depth, which also influences the detailed characteristics of the wave instabilities.

The sensitivity of $U_0(z)$ to Δz is caused by the way in which MITgcm distributes wind-driven momentum. The wind stress, τ_{wind}, has units of $\mathrm{N\,m^{-2}}$ and represents the wind

Table 3.1: List of sensitivity runs and parameter settings

Group	**Run**	**Vertical Mixing**	Δx **(m)**	Δz **(m)**	A_h **(m^2s^{-1})**	A_v **(m^2s^{-1})**
1	C1	Constant	10	0.5	10^{-5}	10^{-5}
	C2			1		
	C3			2		
2	C1	Constant	10	0.5	10^{-5}	10^{-5}
	C4				10^{-3}	10^{-3}
	C5				10^{-1}	10^{-1}
3	K1	KPP	10	0.5	10^{-5}	10^{-5}
	K2			1		
	K3			2		
4	K4	KPP	5	0.5	10^{-5}	10^{-5}
	K1		10			
	K5		25			
	K6		50			
5	K7	KPP	10	0.5	10^{-6}	10^{-5}
	K1				10^{-5}	
	K8				10^{-3}	
	K9				10^{-1}	
6	K10	KPP	10	0.5	10^{-5}	10^{-6}
	K1					10^{-5}
	K11					10^{-3}
	K12					10^{-1}

Table 3.2: List of vertical grids for sensitivity runs

Grid	Δz_1 **(m)**	Δz_2 **(m)**	nz
1	0.5	2	750
2	1	4	375
3	2	4	225
4	4	4	150

Δz_1 is the vertical grid size for the fluid in the upper 300 m, Δz_2 is the vertical grid size for the fluid in the lower 300 m. nz is the total number of grid points in the vertical.

force per unit area. The total momentum input from the wind can be expressed as

$$P_{\text{wind}} = \int_0^T F_{\text{wind}}(t)\,\mathrm{d}t = L_x L_y \int_0^T \tau_{\text{wind}}(t)\,\mathrm{d}t,$$

where L_x and L_y are the horizontal dimensions of the computational domain. In the 2-D configuration considered here, L_y is equal to Δy. Therefore, the total momentum input from the wind is independent of Δz, and consistent across the cases. To investigate why $U_0(z)$ depends strongly on Δz, assume that the fluid is inviscid; that is, the effect of the vertical eddy viscosity is neglected. Under a constant wind stress, τ_{wind}, the wind-induced acceleration in the uppermost grid cell can be written as

$$a_{\text{wind}} = \frac{\tau_{\text{wind}}}{\rho_0 \Delta z}.$$

Consequently, the wind-induced velocity in the uppermost grid cell also scales inversely with Δz. This result closely matches the behaviour shown in panel (d) of Figure 3.2, indicating that $A_v = 10^{-5}\ \mathrm{m^2\,s^{-1}}$ is too weak to propagate momentum downward effectively. This further suggests that, when vertical mixing is weak enough to be neglected, although the total momentum input from the wind is fixed, its vertical distribution depends strongly on Δz.

In Group 3 (cases K1–K3), the KPP mixing scheme is used, with grid parameters corresponding to those in C1–C3 for direct comparison. The simulation results are shown in Panels (e)–(g) of Figure 3.2. Turbulence is parameterized by the KPP scheme, facilitating the more effective downward propagation of momentum into the ocean interior. This leads to a smooth wind-driven current velocity profile, as depicted in Panel (h). Similar to cases

with constant diffusion parameters, the top-layer wind-driven velocity decreases as the grid size increases from $\Delta z = 0.5$ to 2 m. However, because the KPP scheme distributes momentum transfer effectively, the vertical profiles of wind-driven currents remain largely consistent across vertical grid resolutions. Wave behaviour is also similar across the cases.

Group 2 (cases C1, C4, and C5) is designed to evaluate whether increasing the vertical and horizontal diffusive parameter A_v and A_h can reproduce the background velocity profiles and wave's evolution observed in the KPP results. Constant $A_h = A_v = 10^{-5}$, 10^{-3}, and $10^{-1}\,\mathrm{m^2/s}$ are applied, and the results at $t = 0.7$ h are shown in Figure 3.3. The results indicate that as A_v and A_h increases, wind-driven momentum propagates more effectively into the deeper layer, as evidenced by the gradually smaller wave-induced velocity u_b near the surface and the smaller vertical gradient. When $A_h = A_v = 10^{-1}\,\mathrm{m^2/s}$ (Panel c), the wave exhibits weak adjustment, which is similar to the evolution in the KPP results (Figure 3.2 e). However, applying large, spatially uniform eddy diffusivity and viscosity of order $10^{-1}\,\mathrm{m^2/s}$ throughout the computational domain leads to an overly weak u_b throughout the water column compared with the KPP results, indicating excessive vertical viscous mixing.

Therefore, constant diffusivity parameters are not an appropriate tool for studying the effect of wind on internal solitary waves due to the difficulty of accurately representing the vertical turbulence fluxes and their sensitivity to vertical grid spacing. Applying KPP as the vertical turbulent scheme is a better approach for this physical process.

3.2.2 Grid Size

The sensitivity of the KPP scheme to vertical grid size has been evaluated in Group 3 in Section 3.2.1, as shown in Figure 3.2 (e)-(g). The results show that the scheme is not sensitive to variations in vertical grid size for the case of wind-driven turbulence, with $\Delta z = 0.5 \sim 2$ m.

To determine the optimal horizontal grid size for the simulation, Group 4 experiments are conducted with a fixed vertical grid size of $\Delta z = 0.5$ m and varying horizontal grid sizes of $\Delta x = 5$, 10, 25, and 50 m. The results are relatively insensitive to Δx, except that smaller Δx values can resolve finer wave structures. The results shown in Figure 3.4 indicate that, at $\Delta x = 5$ m (Panel a), the simulation resolves small trailing waves. At $\Delta x = 10$ m (Panel b) and $\Delta x = 25$ m (Panel c), the simulations capture only the leading wave and the secondary wave. At $\Delta x = 50$ m (Panel d), the horizontal resolution is too coarse to resolve even the secondary wave, resulting in a significant loss of important

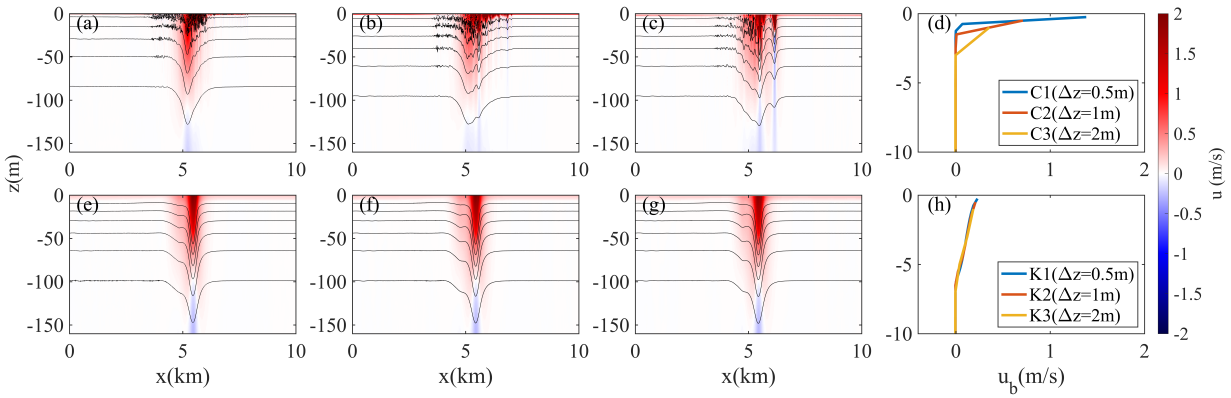


Figure 3.2: Sensitivity tests for Groups 1 and 3 at $t = 0.7$ h. Shading is the horizontal velocity fields, and lines are the density contours. (a)–(c) results for cases C1–C3 with constant diffusivity parameters; (d) vertical profiles of background currents for cases C1–C3; (e)–(g) results for cases K1–K3 with the KPP scheme; (h) vertical profiles of background currents for cases K1–K3.

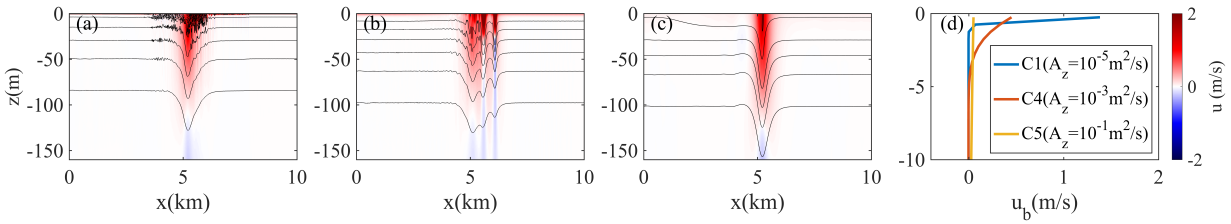


Figure 3.3: Sensitivity tests for Group 2 at $t = 0.7$ h: (a)–(c) results for cases C1,C4,C5 with constant diffusivity parameters; (d) vertical profiles of background currents for cases C1,C4,C5.

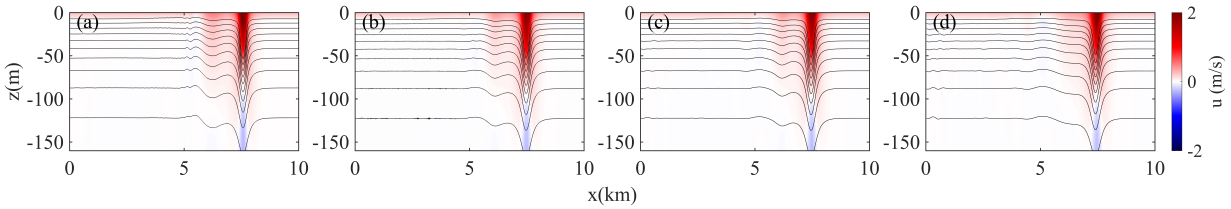


Figure 3.4: Sensitivity tests for Group 4 at $t = 1\,\mathrm{h}$ with $\Delta z = 0.5\,\mathrm{m}$: (a) K4 ($\Delta x = 5\,\mathrm{m}$), (b) K1 ($\Delta x = 10\,\mathrm{m}$), (c) K5 ($\Delta x = 25\,\mathrm{m}$), (d) K6 ($\Delta x = 50\,\mathrm{m}$).

features. Given the available computational resources, $\Delta x = 5\,\mathrm{m}$ is chosen as the horizontal grid size in this study.

3.2.3 Diffusion Parameters

In the MITgcm, the background diffusion parameters A_h and A_v can be tuned to control the flow characteristics. The KPP-computed vertical diffusivity and viscosity will then be added to the prescribed background A_v. The background coefficients therefore set the baseline level of interior mixing in regions without shear instability and can affect the simulated flow fields. To evaluate the sensitivity of the simulation results to these background parameters, Groups 5 and 6 were designed to investigate the effects of A_h and A_v, respectively.

The results for Group 5 are presented in Figure 3.5 (a)-(d), with A_v fixed at $10^{-5}\,\mathrm{m^2/s}$ and A_h varied across $10^{-6}, 10^{-5}, 10^{-3}, 10^{-1}\,\mathrm{m^2/s}$. The wave evolution results at $t = 1\,\mathrm{h}$ are nearly identical, which indicates that the variations in the horizontal diffusivity A_h have negligible effects on wave evolution.

In contrast, the results for Group 6, shown in Figure 3.5 (e)-(h), reveal that A_v has a more pronounced impact. In this group, A_h is fixed at $10^{-5}\,\mathrm{m^2/s}$, while A_v is varied across $10^{-6}, 10^{-5}, 10^{-3}$, and $10^{-1}\,\mathrm{m^2/s}$. The results demonstrate that significant changes in wave evolution occur only when $A_v = 10^{-1}\,\mathrm{m^2/s}$. For $A_v \leq 10^{-3}\,\mathrm{m^2/s}$, the wave evolution remains nearly identical across cases. Therefore, the vertical diffusivity A_v only significantly influences wave evolution when it reaches a high value of $O(10^{-1})\,\mathrm{m^2/s}$, which is unrealistically large for internal solitary wave studies.

These findings suggest that the KPP scheme is relatively robust to changes in background diffusivity parameters, making it unnecessary to frequently adjust A_h and A_v in simulations. Consequently, the values $A_h = 10^{-5}\,\mathrm{m^2/s}$ and $A_v = 10^{-5}\,\mathrm{m^2/s}$ are adopted for subsequent experiments.

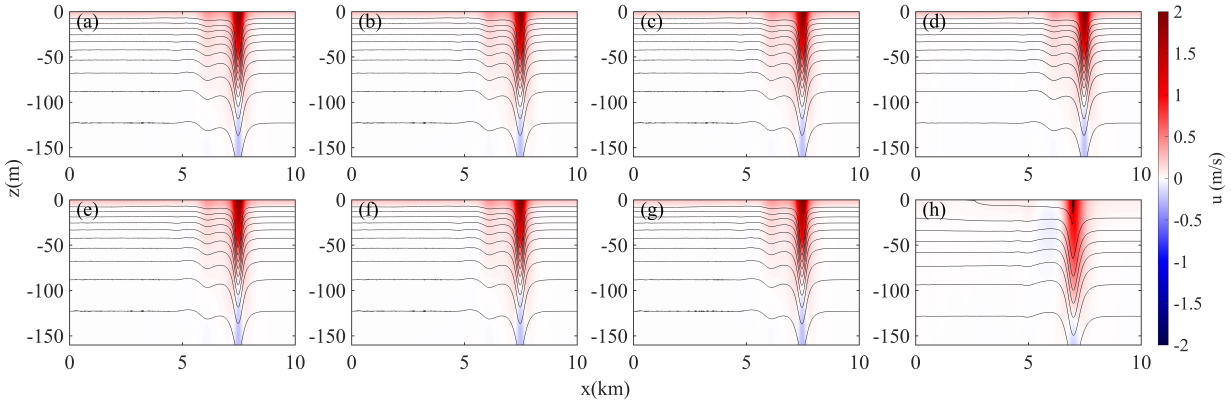


Figure 3.5: Sensitivity tests on background diffusivity for the KPP cases at $t = 1\,\mathrm{h}$: (a)-(d) Group 5 with $A_v = 10^{-5}\,\mathrm{m}^2/\mathrm{s}$: (a) $A_h = 10^{-6}\,\mathrm{m}^2/\mathrm{s}$ (K7), (b) $A_h = 10^{-5}\,\mathrm{m}^2/\mathrm{s}$ (K1), (c) $A_h = 10^{-3}\,\mathrm{m}^2/\mathrm{s}$ (K8), (d) $A_h = 10^{-1}\,\mathrm{m}^2/\mathrm{s}$ (K9). (e)-(h) Group 6 with $A_h = 10^{-5}\,\mathrm{m}^2/\mathrm{s}$: (e) $A_v = 10^{-6}\,\mathrm{m}^2/\mathrm{s}$ (K10), (f) $A_v = 10^{-5}\,\mathrm{m}^2/\mathrm{s}$ (K1), (g) $A_v = 10^{-3}\,\mathrm{m}^2/\mathrm{s}$ (K11), (h) $A_v = 10^{-1}\,\mathrm{m}^2/\mathrm{s}$ (K12).

Chapter 4

Results

4.1 Introduction

Many studies have examined ISWs in coastal regions such as the northern South China Sea, where waves generated near Luzon Strait propagate westward toward Dongsha Atoll and the continental slope (Alford et al., 2015). These studies have documented a range of ISW behaviors during shoaling, such as polarity change (Zhao et al., 2003), fission (Bai et al., 2019), interactions with shear currents (Lien et al., 2012), and dissipation (Chang et al., 2021). However, most previous work has focused on ISW evolution under the influence of background currents and bathymetry. At the same time, the role of external forcing, such as transient surface wind forcing, remains less well understood.

Wind forcing can modify the background conditions experienced by ISWs. Surface winds can generate near-surface turbulence, deepen the mixed layer, and introduce additional shear in the upper water column (Glenn et al., 2016; Miles et al., 2017; Foltz, 2019). Recent observations have suggested that wind forcing and ISWs act together to enhance local mixing (Magalhaes et al., 2025). Field observations of this coupled process, however, are limited by inadequate near-surface data. In addition, in complex oceanic environments, observational studies often cannot fully isolate wind-induced and wave-induced motions from the broader ocean system. Therefore, numerical simulations provide a controlled framework in which this important but underexplored question can be examined separately.

In this chapter, the response of an ISW to surface wind forcing is investigated using a series of idealized simulations. Cases with positive and negative constant wind stress

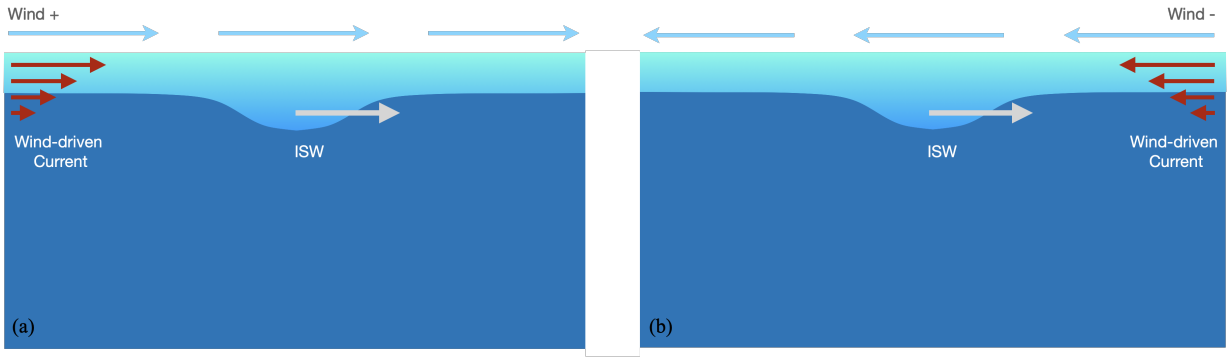


Figure 4.1: Diagram illustrating the physical process of wind's influence on internal solitary waves. (a) Wind direction aligns with the wave propagation direction. (b) Wind direction opposes the wave propagation direction.

are first conducted. The effects of wind strength and wind ramping are then examined to determine how the magnitude and time dependence of the applied forcing influence wave evolution. The simulations aim to identify how wind affects ISW propagation and structure.

4.2 Model Configuration

The physical processes simulated in this chapter are illustrated in Figure 4.1, which presents two cases: (a) wind propagating in the same direction as the wave and (b) wind propagating in the opposing direction. To investigate the processes, the model is set up as follows.

Based on the sensitivity tests described in Section 3, the simulations utilize a uniform horizontal grid spacing of $\Delta x = 5$ m, and a non-uniform vertical grid. The vertical resolution is set to $\Delta z = 0.5$ m from $z = -300$ m to $z = 0$ m and $\Delta z = 2$ m from $z = -600$ m to $z = -300$ m. The time step Δt is set to 0.2 s. The simulation domain extends $L = 40$ km horizontally, with a total water depth of $H = 600$ m. The KPP mixing scheme is applied to parameterize the vertical turbulent flux within the domain. The background eddy viscosity ν_h, ν_v and diffusivity κ_h, κ_v parameters are all set to 10^{-5} m^2/s.

The initial fields obtained from the numerical solution of the DJL equation (Eq. 3.2) and the stratification equation (Eq. 3.1) are identical to those in Section 3.

To investigate the impact of wind strength, direction, and patterns on internal waves, a group of experiments is designed with the parameters provided in Table 4.1. In all exper-

iments, the wind stress is spatially uniform in the x direction. Constant wind conditions are applied in experiments P1, P2, P3, and N1. Temporal variations of the surface wind stress in experiments P1-up and P1-up-down are shown in Figure 4.2.

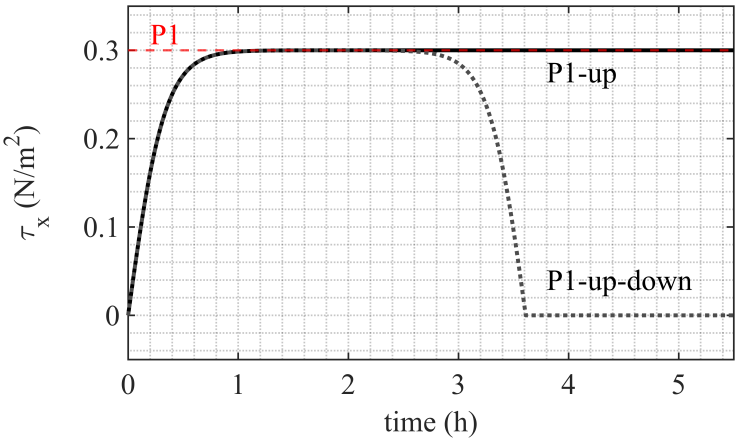


Figure 4.2: The wind patterns in P1, P1-up and P1-up-down.

4.3 Baseline Constant Wind Stress Simulations

In this section, we present the evolution of the ISW under constant wind stress. We first define several variables and sign conventions used in the following analysis. Wind stress is denoted by τ_x, where $\tau_x > 0$ indicates that the wind aligns with the wave propagation direction, while $\tau_x < 0$ indicates the opposite direction. The horizontal velocity is denoted by u. The background flow velocity, U_b, is measured at $x = 35$ km, and U_b^0 denotes its surface value at $z = 0$. Similarly, u_c denotes u at the wave centre x_c and u_c^0 represents its surface value. x_c is defined as the location of the maximum vertical displacement. The wave propagation speed c is computed using a central difference approximation of x_c in time.

4.3.1 Positive Constant Wind Stress

Figure 4.3 displays results of the case P1, which shows the evolution of an ISW under a constant positive wind condition $\tau_x = 0.3$ N/m^2. The initial profile for the stable ISW is shown in Panel (a), where the wind has not affected the wave field. Panels (b)-(e)

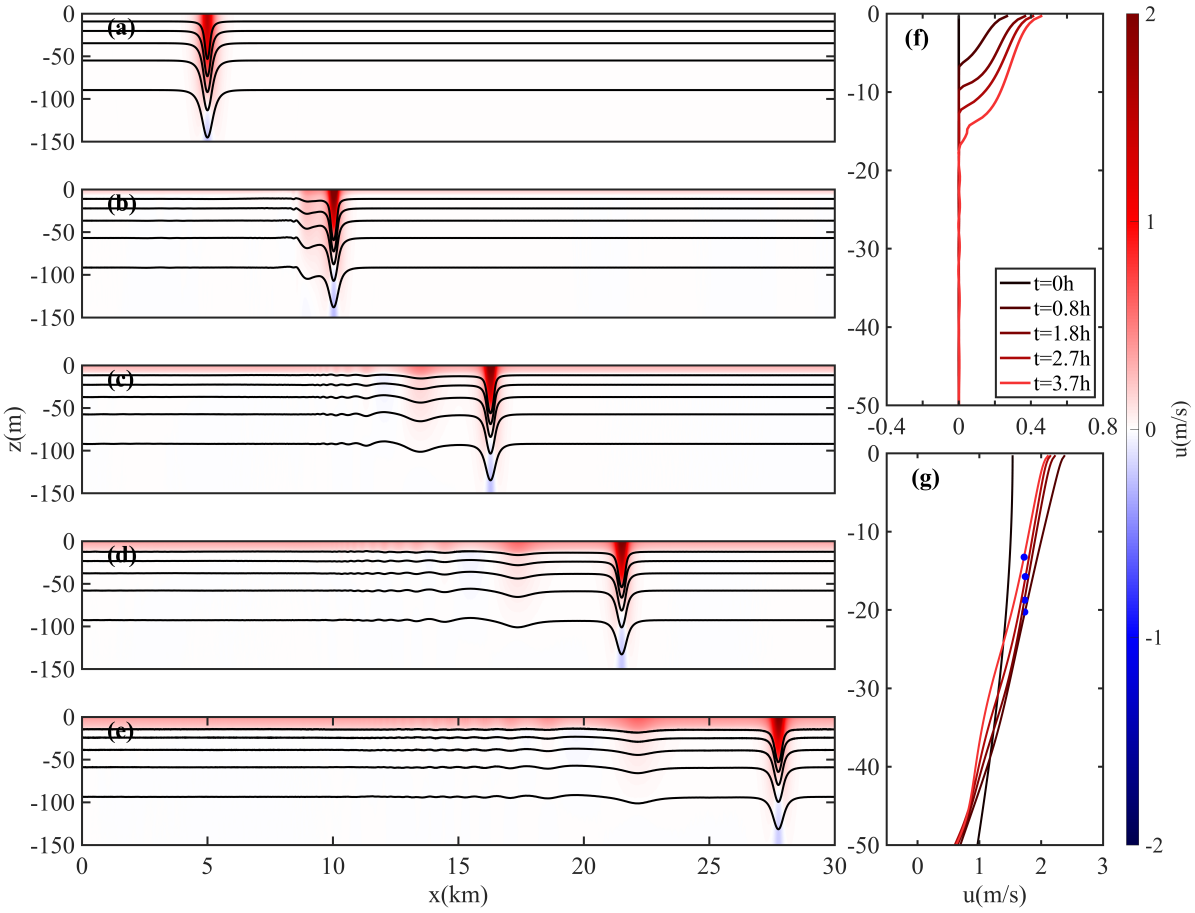


Figure 4.3: Evolution process for Case P1 with constant $\tau_x = 0.3$ N/m^2: (a)-(e) The horizontal component of velocity u in the top 150 m is shaded, with five density contours shown in black at $t = 0$ h, 0.8 h, 1.8 h, 2.7 h, and 3.7 h. (f) The vertical profile of the wind-driven background current U_b, obtained by sampling u at $x = 35$ km; the black line represents the initial state. (g) The vertical profile of u_c at the trough of the leading wave at the same times as in (f); the blue dots represent the location where $u = c$.

Table 4.1: List of runs and parameter settings

Case	**Maximum Wind Stress (N/m^2)**	**Maximum Wind Speed (m/s)**	**Direction**	**Pattern**
P1	0.3	13.7	+	constant
P2	0.6	19.4	+	constant
P3	0.15	9.7	+	constant
N1	0.3	13.7	−	constant
P1-up	0.3	13.7	+	temporally varying
P1-up-down	0.3	13.7	+	temporally varying

Direction "+" means that the wind direction is aligned with the wave propagation direction, while direction "−" means that the wind direction is opposite to the wave propagation direction. Wind pattern "constant" refers to steady wind stress. Cases P1-up and P1-up-down have wind stress varying over time, as shown in Figure 4.2. The wind speed is estimated using the bulk aerodynamic formulation following previous wind-stress calculation (Pickett and Paduan, 2003).

present the wave fields from $t = 0.8$ h to $t = 3.7$ h. The wind induces an accelerated background current U_b, with the vertical profile at different times shown in Panel (f). The background current affects only the top 20 m of the water up to $t = 3.7$ h, being strongest at the surface and decreasing with depth. The wind also leads to the formation and deepening of a mixed layer. As the background conditions evolve continuously, the leading internal solitary wave stays unstable and adjusts its shape. Panel (g) shows that during the evolution, u_c, the horizontal velocity at the wave centre, near the surface, increases rapidly after the simulation begins. This increase creates a region where $|u| > |c|$ near the surface, as seen in Figure 4.3 (g), a characteristic that is not present in the initial wave field. This can also be visualized in Panels (b)–(e), where a high-momentum region forms at the wave centre. At $t = 0$, the surface velocity at the wave centre is $u_c^0 = 1.53$ m/s. At $t = 0.8$ h, the background current velocity is $U_b^0 = 0.27$ m/s, while the velocity at the wave centre is $u_c^0 = 2.38$ m/s. This indicates that the strong flow at the wave centre is not a result of simple linear superposition of background currents and the initial wave's velocity field, as u_c^0 ($t = 0.8$ h) exceeds the sum of U_b^0 ($t = 0.8$ h) and u_c^0 ($t = 0$). In other words, a nonlinear interaction between the background current and the ISW leads to a concentration of momentum near the surface.

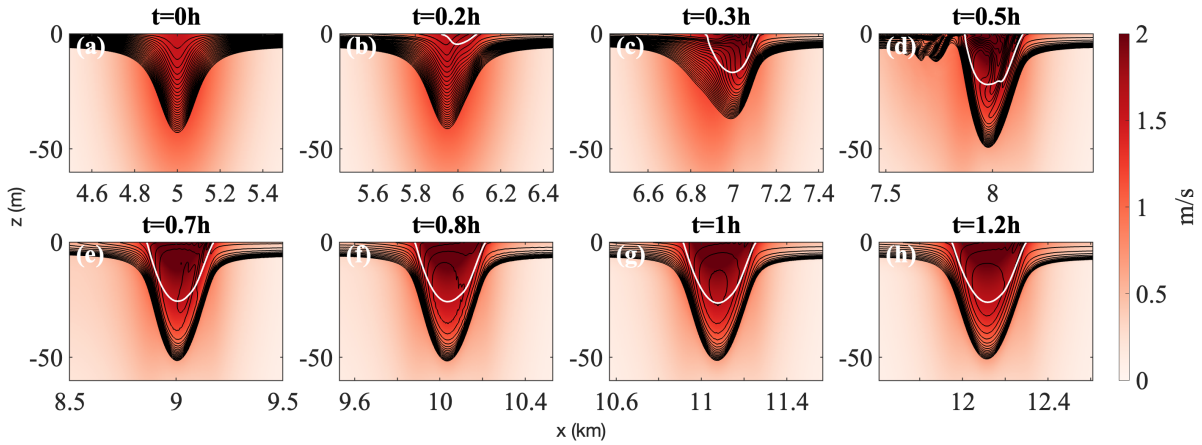


Figure 4.4: A close-up view of the snapshot of u from $t = 0$ to $t = 1.2$ h in the top 60 m, showing only the density contours near the surface. The white lines indicate where $u = c$ and are used as a simple measure of the core thickness d_c.

The entire wave evolution under wind can generally be divided into two stages: the fission phase, where rapid reshaping of the wave occurs due to the onset of wind, and the propagation phase, where the shape of the leading wave remains relatively robust while the wave's amplitude decreases.

Figure 4.4(a)-(d) illustrates the fission process from $t = 0$ h to $t = 0.5$ h. Within the white contours, the fluid particle velocity u exceeds the wave propagation speed c. Therefore, the steepening and overturning of the isopycnals occur at the rear of the wave (Figure 4.4c). Denser fluid then penetrates relatively lighter fluid layers, leading to the instability observed at the wave centre (Figure 4.4d). During this stage, the key characteristics of the wave also evolve significantly (Figure 4.5). Wave amplitude A_{max} is defined as the maximum displacement of the isopycnals at each time, and core thickness d_c is defined as the maximum depth at the location where $u = c$, which is used to assess the vertical extent of convective instability. Note that the $u = c$ contour in Figure 4.4 does not represent the lower boundary of the core; the core structure extends below the white lines. The amplitude of the leading wave decreases rapidly (panel a). This decrease can be explained by the fission process, during which part of the leading-wave energy is transferred to the trailing waves. In the presence of wind-induced shear currents, the core forms and grows rapidly (panel b). During this stage, the propagation speed of the leading wave increases from $c = 1.58$ m/s to $c = 1.73$ m/s.

After $t = 0.5$ h, no further overturning or fission occurs, indicating the start of the

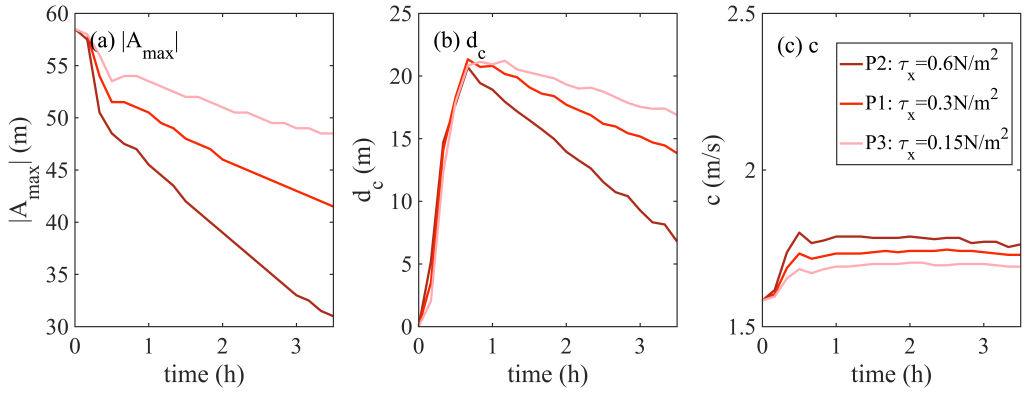


Figure 4.5: Evolution of key characteristics in Cases P1, P2, and P3: (a) maximum amplitude $|A_{max}|$, (b) core thickness d_c, (c) propagation speed c.

second stage, the propagation phase. Figure 4.4(e)-(h) shows that as the leading wave continues to move forward, the instability region lags and trailing waves form, as observed in Figure 4.3(c). Here, the instability region refers to the localized region of overturned density structure. The overturning at the wave centre intensifies mixing, leading to the formation of a core of fluid with nearly uniform density, indicated by the closed density contours (Figure 4.4f). However, this stratification structure is not stable, suggesting that the system cannot reach equilibrium under wind forcing. Figure 4.5 shows that, starting from $t = 0.67$ h, the thickness of the wave core decreases significantly over time, while the amplitude of the leading wave continues to decrease, but at a slower rate than during the first stage. The propagation speed c remains nearly constant during this phase, although the background current velocity continuously increases with time (Figure 4.3f). This nearly constant value of c may result from a balance between the increasing background current and the decreasing wave amplitude, which have opposite effects on c.

Under the strong shear shown in Figure 4.3(f), no numerical solutions of the DJL equation exist for a stable internal solitary wave. Similarly, Walter et al. (2016) found that the DJL model fails to accurately describe nonlinear internal solitary wave trains in the presence of strong shear. This confirms the limitations of the DJL theory and shows that the MITgcm model is needed for more accurate simulations.

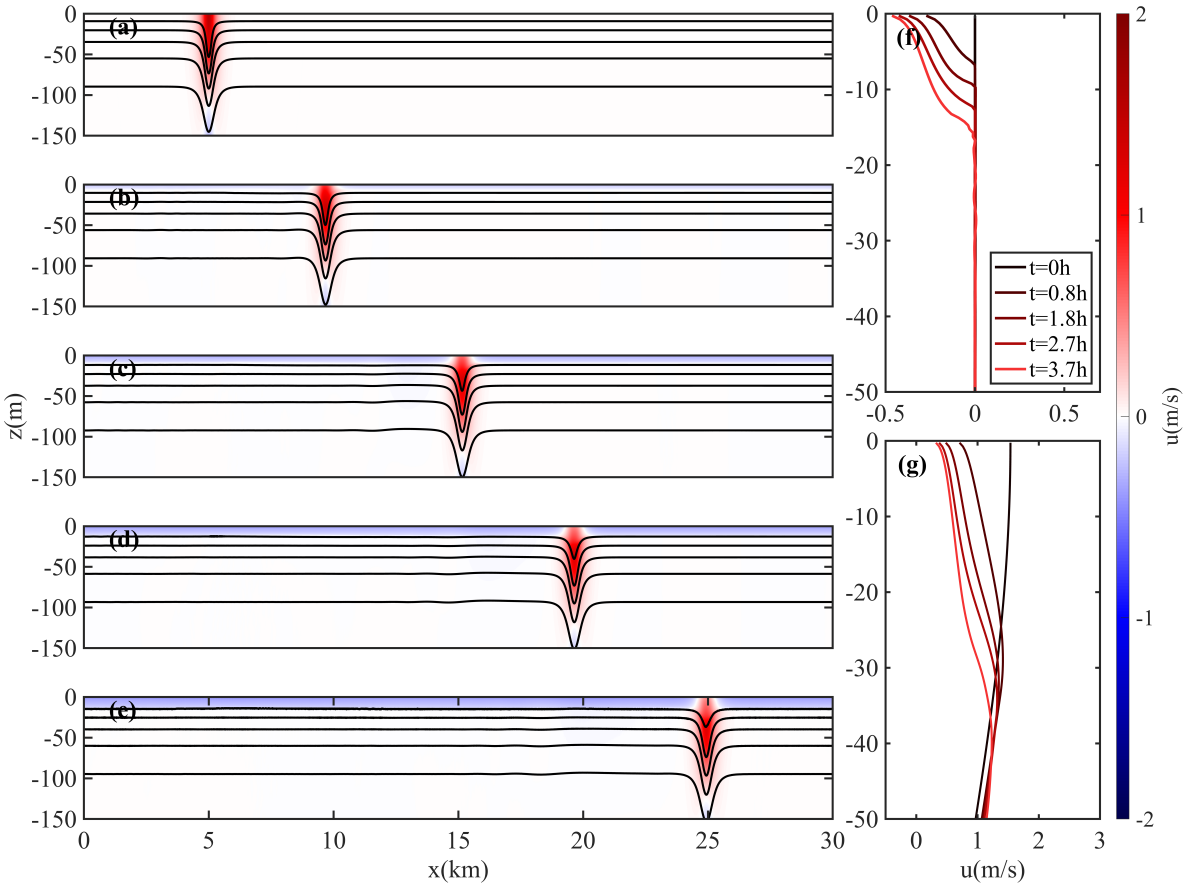


Figure 4.6: Evolution process for Case N1 with constant $\tau_x = -0.3$ N/m^2: (a)-(e) The horizontal component of velocity u in the top 150 m is shaded, with five density contours shown in black at $t = 0$ h, 0.8 h, 1.8 h, 2.7 h, and 3.7 h. (f) The vertical profile of the wind-driven background current U_b, obtained by sampling u at $x = 35$ km; the black line represents the initial state. (g) The vertical profile of u_c at the trough of the leading wave at the same times as in (f).

4.3.2 Negative Constant Wind Stress

Figure 4.6 displays the wave evolution in Case N1, with $\tau_x = -0.3$ N/m^2, opposing the direction of wave propagation. Compared with Case P1, reversing the wind direction changes the direction of the background flow while preserving its velocity magnitude (panel f). Under negative wind forcing, the wave exhibits only a weak adjustment in shape, and the amplitude of the leading wave remains nearly constant. Panel (g) presents the horizontal velocity profiles $u_c(z)$ at the wave trough. The negative wind reduces the near-surface u_c. Near the surface, U_b and u_c have the same sign of vertical shear, $\partial u/\partial z$, down to approximately $z \approx -30$ m.

Wind affects the wave field by both accelerating the background current and deepening the mixed layer. We denote the background velocity and density profiles obtained from the MITgcm by $U_b(z,t)$ and $\rho_b(z,t)$, respectively. To separately analyze the effects of background velocity and stratification on wave evolution, the DJL equation is solved numerically to obtain solitary wave solutions under four combinations of background velocity $U(z,t)$ and stratification $\rho(z,t)$, C1-C4:

- **C1:** $U(z,t) = U_b(z,t)$ and $\rho(z,t) = \rho_b(z,t)$, which assess the combined effect of background velocities and density on wave evolution.
- **C2:** $U(z,t) = U_b(z,0) = 0$ and $\rho(z,t) = \rho_b(z,t)$, which represent the case of no background flow and examine how changes in stratification affect wave evolution.
- **C3:** $U(z,t) = U_b(z,t)$ and $\rho(z,t) = \rho_b(z,0)$, which examine the influence of wind-driven current on wave evolution.
- **C4:** $U(z,t) = 0$ and $\rho(z,t) = \rho_b(z,0)$, which serve as a reference case that represents the situation without wind.

In conditions C1 and C3, the $U(z,t)$ profile is fitted to $U_b(z,t)$ using:

$$U(z,t) = \sum_{i=1}^{5} a_i \exp\left(-(b_i z + c_i)^2\right) + d \tag{4.1}$$

Because $U_b(z,t)$ varies rapidly with depth, it is fitted to ensure smooth U_z and U_{zz} for the DJL calculation. For conditions C1 and C2, the $\rho(z,t)$ profile is obtained by linear interpolation of $\rho_b(z,t)$ to fit in the DJL computational grids. Both $\rho_b(z,t)$ and $U_b(z,t)$ are extracted from MITgcm.

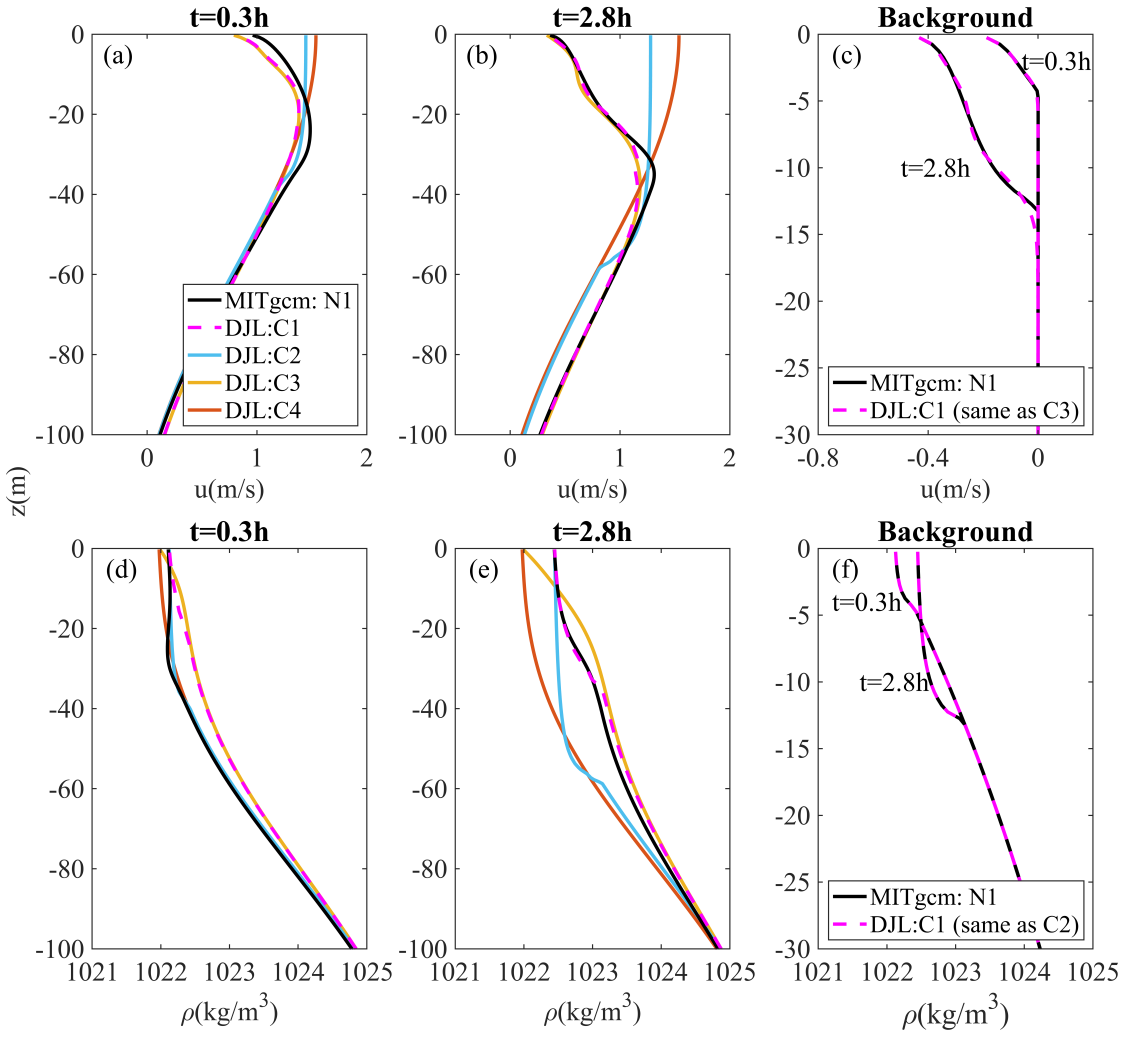


Figure 4.7: DJL solutions at the leading wave centre under conditions C1-C4 and MITgcm solutions under N1. (a) Velocity profiles at the wave centre $u_c(z)$ at $t = 0.3\,\mathrm{h}$. (b) Same as (a), but at $t = 2.8\,\mathrm{h}$. (c) Background velocity profiles U_b at $x = 35\,\mathrm{km}$ (a region without waves) from the MITgcm at $t = 0.3\,\mathrm{h}$ and $t = 2.8\,\mathrm{h}$, with the fitted background velocity profiles used in DJL cases C1 and C3 superimposed. In DJL cases C2 and C4, $U_b(z) = 0$ and is not shown. (d) Density profiles at the wave centre $\rho_c(z)$ at $t = 0.3\,\mathrm{h}$. (e) Same as (d), but at $t = 2.8\,\mathrm{h}$. (f) Background density profiles ρ_b from the MITgcm at $t = 0.3\,\mathrm{h}$ and $t = 2.8\,\mathrm{h}$, with the interpolated background density profiles used in DJL cases C1 and C2 superimposed. In DJL cases C3 and C4, background density profile is the initial density profile applied in MITgcm and not shown.

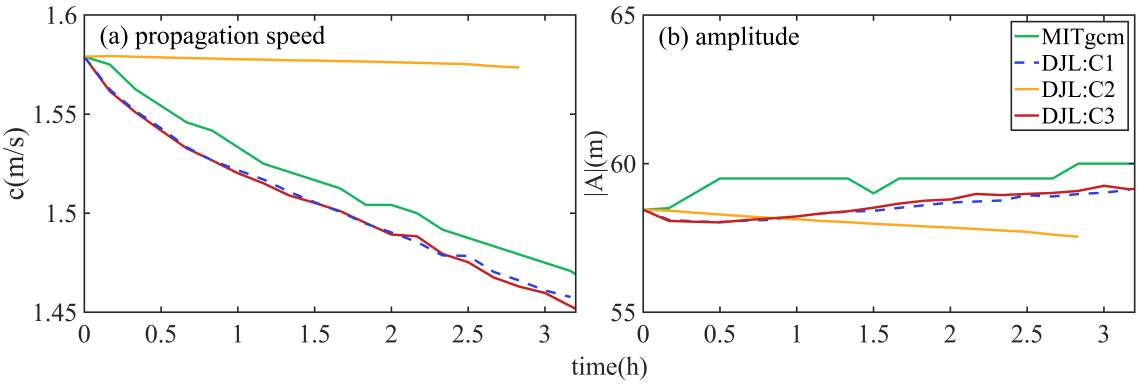


Figure 4.8: DJL solutions under conditions C1-C3 and the MITgcm solution for the temporal evolution of (a) the propagation speed c and (b) the amplitude of leading wave $|A|$.

The numerical solutions of the DJL equation are computed from $t = 0$ to $t = 2.8$ h at the time interval same as MITgcm outputs. Beyond $t = 2.8$ h, the DJL equation under conditions C1 and C3 fails to converge when the background shear becomes too strong. Figure 4.7 shows the velocity and density profiles at the wave trough, $u_c(z)$ and $\rho_c(z)$, from the DJL solutions, as a reflection of the wave's structure.

At $t = 0.3$ h, a discrepancy is observed in the upper 50 m between the results from the DJL C1 and the MITgcm, although their background conditions are nearly identical, as shown in Panels (c) and (f). In particular, the MITgcm results remain closer to the initial ISW state represented by C4. This discrepancy arises because the DJL equation describes only the steady-state structure of an ISW under a prescribed background condition. In contrast, in the MITgcm equipped with the KPP scheme, the background current and density fields evolve. Consequently, the results in the MITgcm reflect the cumulative effects of the changing background conditions over the preceding period.

By $t = 2.8$ h, $u_c(z)$ and $\rho_c(z)$ in DJL C1 generally agree with the MITgcm results, except near $z \approx -40$ m. This agreement suggests that the DJL equation can reliably capture the key characteristics of an ISW after a longer adjustment period. We therefore use the DJL results for further analysis at this time.

To examine the effect of the wind-induced mixed layer, we compare C3 (shear only) with C1 (mixing and shear), and C2 (mixing only) with C4 (no mixing and no shear), at $t = 2.8$ h. The mixed-layer profile is shown in Panel (f). The profiles of $u_c(z)$ at the wave trough are very similar between C1 and C3, indicating that the mixed layer has little influence on the vertical structure of $u_c(z)$ in the presence of background shear. In

contrast, clear differences are observed between C2 and C4. In C2, $u_c(z)$ is nearly uniform within the mixed layer, a feature that is absent in C4. These results suggest that, in the absence of background shear, the wind-induced mixed layer modifies the wave momentum distribution, leading to a nearly uniform $u_c(z)$ within the mixed layer. However, when background shear is present, it dominates the wave's structure, rendering the mixed layer's influence negligible.

Baroclinic vorticity generation can explain the role of the mixed layer in shaping the near-surface velocity structure. Under the Boussinesq and inviscid approximations, baroclinic vorticity generation is associated with horizontal density gradients, ρ_x. Within a surface mixed layer, the wave-induced ρ_x is negligible, so little baroclinic vorticity is generated and the existing vorticity is approximately materially conserved. Consequently, the near-surface vorticity, approximated by $\partial u/\partial z$, largely reflects the ambient mixed-layer vorticity. This explains the behaviour of cases C1 and C2. In C2, the absence of background shear results in $\partial u/\partial z \approx 0$ at the wave centre, as shown in Fig. 4.7(b), whereas in C1, the nonzero background vorticity is approximately retained within the wave. Case C3 has no mixed layer, allowing baroclinic vorticity generation near the surface. However, the generated vorticity is small relative to the pre-existing background vorticity, so the near-surface shear remains similar to that in C1.

Figure 4.8(a) shows the propagation speeds c. Under DJL C2 (mixing only), c remains nearly unchanged. This suggests that the deepening of the mixed layer has only a minimal effect on c. In contrast, the values of c under DJL C1 and C3 are similar and exhibit the same decreasing trend as the MITgcm solution. Figure 4.8(b) shows the temporal evolution of the wave amplitude under the various conditions. Overall, the amplitudes obtained from all models are in close agreement ($A \approx -59$ m). Thus, under negative wind forcing, wind-induced background shear plays a dominant role over changes in stratification in modulating the propagation speed of the evolving ISW.

4.4 Parameter Influence Experiments

4.4.1 Wind Strength

To examine the impact of wind strength on the ISWs, cases P2 and P3 are conducted to study wave behavior under different wind conditions: strong wind ($\tau_x = 0.6$ N/m^2) and weak wind ($\tau_x = 0.15$ N/m^2). The results are presented in Figures 4.9 and 4.10, respectively. Larger wind stress generates a much stronger background current. At $t = 3.7$

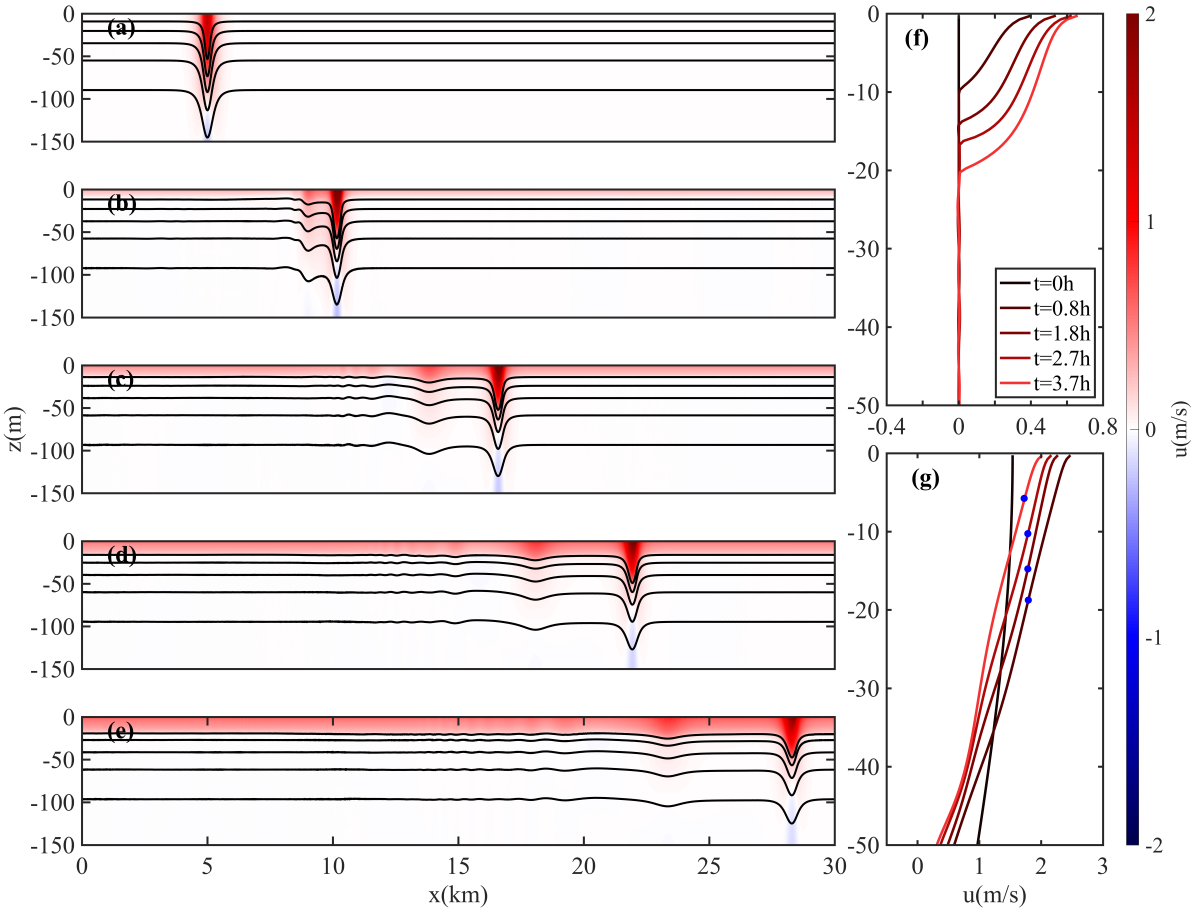


Figure 4.9: Evolution process for Case P2 with constant $\tau_x = 0.6$ N/m^2: (a)-(e) The horizontal component of velocity u in the top 150 m is shaded, with five density contours shown in black at $t = 0$ h, 0.8 h, 1.8 h, 2.7 h, and 3.7 h. (f) The vertical profile of the wind-driven background current U_b, obtained by sampling u at $x = 35$ km; the black line represents the initial state. (g) The vertical profile of u_c at the trough of the leading wave at the same times as in (f); the blue dots represent the location where $u = c$.

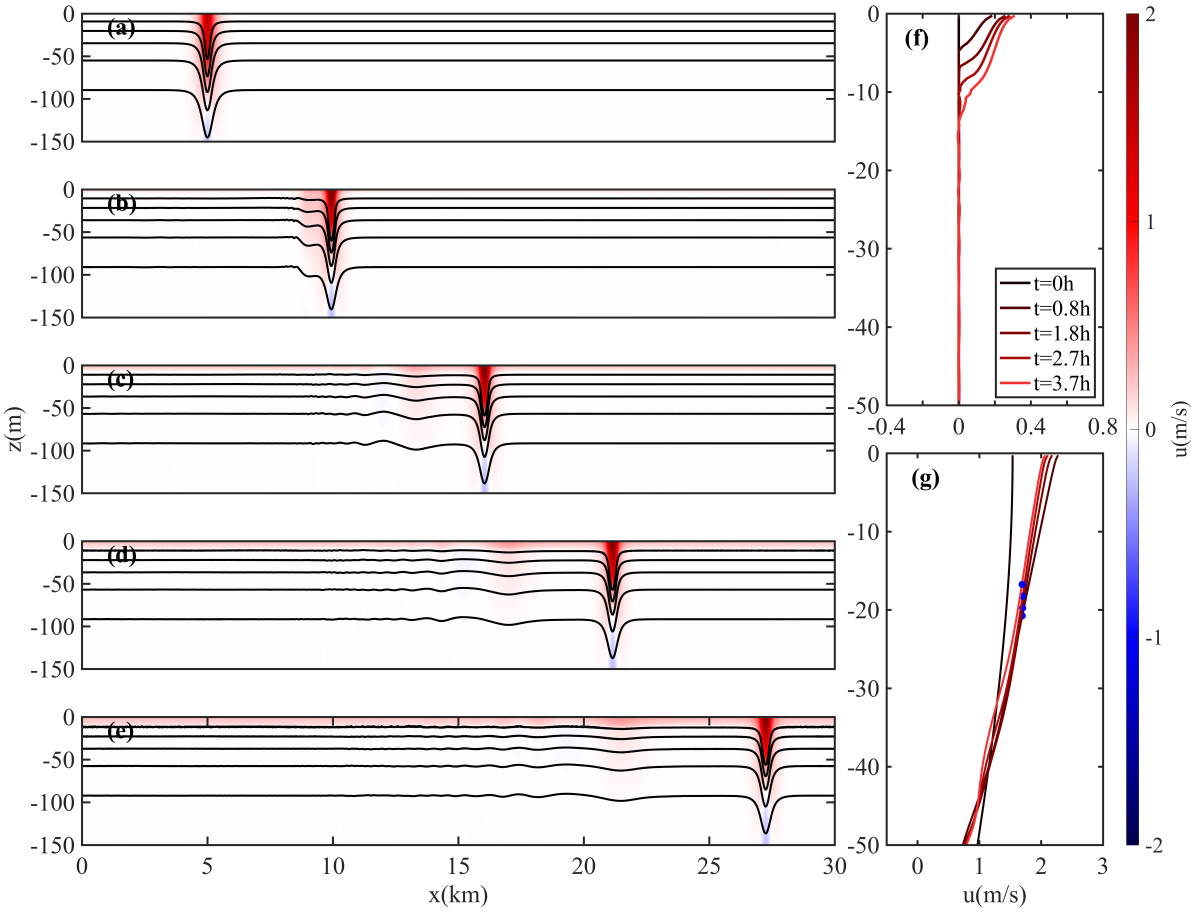


Figure 4.10: Evolution process for Case P3 with constant $\tau_x = 0.15$ N/m^2: (a)-(e) The horizontal component of velocity u in the top 150 m is shaded, with five density contours shown in black at $t = 0$ h, 0.8 h, 1.8 h, 2.7 h, and 3.7 h. (f) The vertical profile of the wind-driven background current U_b, obtained by sampling u at $x = 35$ km; the black line represents the initial state. (g) The vertical profile of u at the wave trough of the leading wave at the same times as in (f); the blue dots represent the location where $u = c$.

h, the surface velocity of background currents U_b^0 reaches 0.30 m/s, 0.46 m/s, and 0.65 m/s for wind stresses of 0.15, 0.3, and 0.6 N/m^2, respectively. The waves' evolution follows the same pattern under all conditions: fission occurs initially, and then the leading wave maintains a robust form with a gradually decreasing amplitude. Differences emerge when comparing the details of the two cases. In the strong wind case P2, fission is more pronounced, evidenced by the leading wave with a smaller amplitude compared to P1 and the secondary wave with a larger amplitude. Additionally, $u_c(z)$ decreases significantly over time after $t = 0.8$ h under strong wind, whereas the decrease is slight under the weak wind case P3(Panel g).

Figure 4.5 provides a direct comparison of the wave quantities. Panel (a) demonstrates that $|A_{max}|$ decreasing rate increases with the wind stress. Panel (b) depicts the temporal evolution of core thickness d_c. In all cases, the d_c reaches the depth of approximately 21 m before decreasing at different rates. Consistent with the findings for $|A_{max}|$, stronger winds lead to a more rapid reduction in d_c due to increased eddy viscous dissipation Panel (c) shows the evolution of propagation speed c. The presence of wind causes the waves to initially adjust their speed to a higher value in accelerating background currents, and then maintain at a consistent level. When wind is in the same direction as the wave, the ISW under strong wind has a higher propagation speed.

4.4.2 Ramp Wind

The previous sections explored the impact of constant wind stress on internal wave fields. When wind stress increases gradually (P1-up) and decreases gradually (P1-up-down), the wave fields evolve differently. Figure 4.2 presents the wind patterns applied in these scenarios, each with a maximum wind stress $\tau_x = 0.3$ N/m^2. The development of the corresponding background conditions is illustrated in Figure 4.11. This figure displays the horizontal background velocity at the surface level U_b^0, and the Mixed Layer Depth (MLD) diagnosed by $T - T_b^0 = -0.2$ °C (de Boyer Montégut et al., 2004). Here, the MLD is used to evaluate the stratification.

Figure 4.12 compares a constant wind scenario (P1) with a gradually increasing wind scenario (P1-up) between $t = 0.5$ h and $t = 1$ h. The difference in u between the two cases is also shown in Figure 4.12 (i)-(l), defined as $u_{\text{P1-up}} - u_{\text{P1}}$, after alignment by x_c. The fission in the case P1-up behave similarly as the case P1, while the wave shape adjustment is weaker. This is because the gradually increasing wind stress causes a delay in the development of the background current compared to the constant wind scenario (Figure 4.11 a). The MLD is also slightly lower than in case P1, but the difference is small (Panel b).

From an energy perspective, the work done by the wind on the water partly increases the KE by inducing shear currents, partly increases the PE by enhancing mixing, while the remainder is dissipated through viscous processes. The gradually increasing wind reduces the cumulative momentum input of wind. Consequently, the kinetic and potential energies cannot reach the same levels as in the P1 case.

Figure 4.13 illustrates the effect of decreasing wind stress by comparing the results of cases P1-up and P1-up-down between $t = 3.8$ h and $t = 4.5$ h. During this period, τ_x in case P1-up remains 0.3 N/m^2, while in case P1-up-down, τ_x has decreased to zero, indicating that the wind has stopped (Figure 4.2). In contrast to case P1-up, where the wave shape remains robust under constant wind stress, case P1-up-down shows different behavior. As the wind stress decreases and the background current slows (Figure 4.14), an adjustment process is triggered, resulting in small trailing waves behind the leading wave. The detailed evolution of this adjustment in case P1-up-down is depicted in Figure 4.16. At $t = 3.8$ h, shortly after the wind stops, instabilities are visible from the wave centre to the rear of the wave (Panel b1). The $|u| > |c|$ region becomes smaller and eventually disappears by the end of the simulation (Panels d2–f2).

The above adjustment, which occurs after the wind stops, can be explained by changes in background flow conditions. During this phase, both the background velocity $U_b(z)$ and vorticity $\partial U_b/\partial z$ near the surface decrease substantially, as shown by comparing $t = 4.5$ h with $t = 3.5$ h in Figure 4.14(a). The new $U_b(z)$ can no longer support the wave structure observed in Figure 4.16(a1), which has high vorticity near the surface at the wave centre, as shown in Panel (a2). Therefore, after the wind stops, the wave gradually adjusts its structure to that shown in Panel (f1), where the near-surface vorticity becomes nearly zero, as shown in Panel (f2).

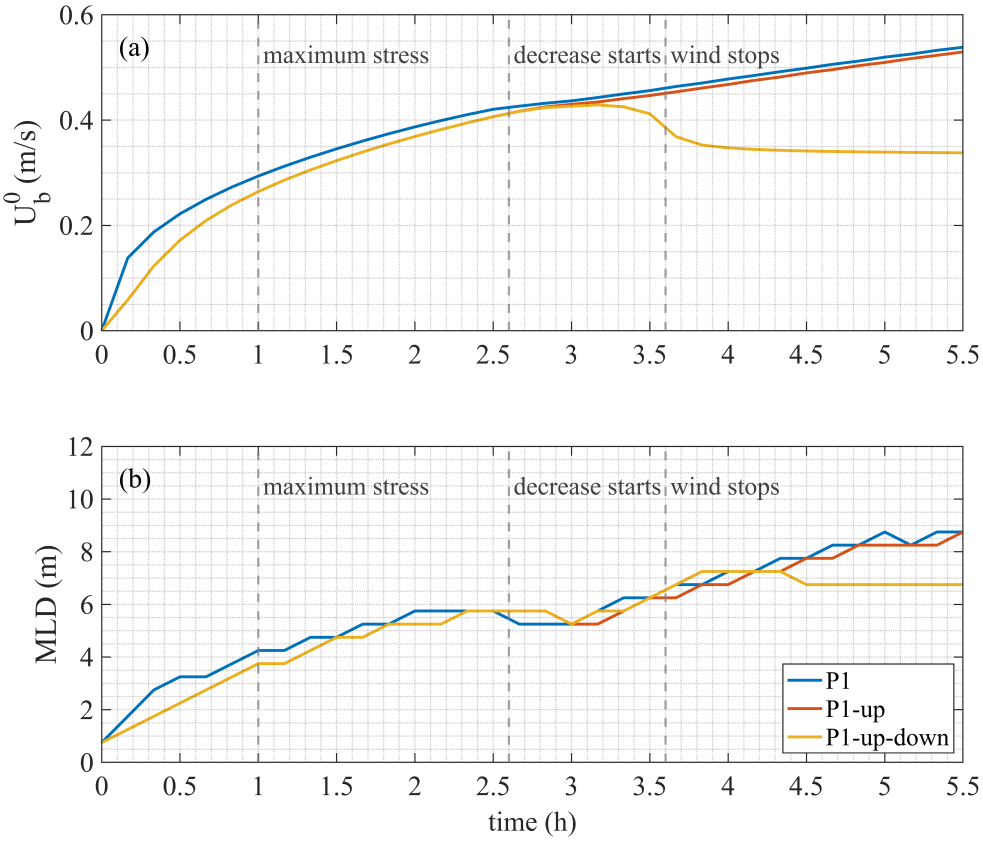


Figure 4.11: Comparison of the evolution of background conditions (a) U_b^0, the velocity of wind-driven currents at the surface; and (b) MLD, the mixed layer depth diagnosed using $T - T_b^0 = -0.2$ °C. The blue, red, and orange lines represent cases P1, P1-up, and P1-up-down, respectively.

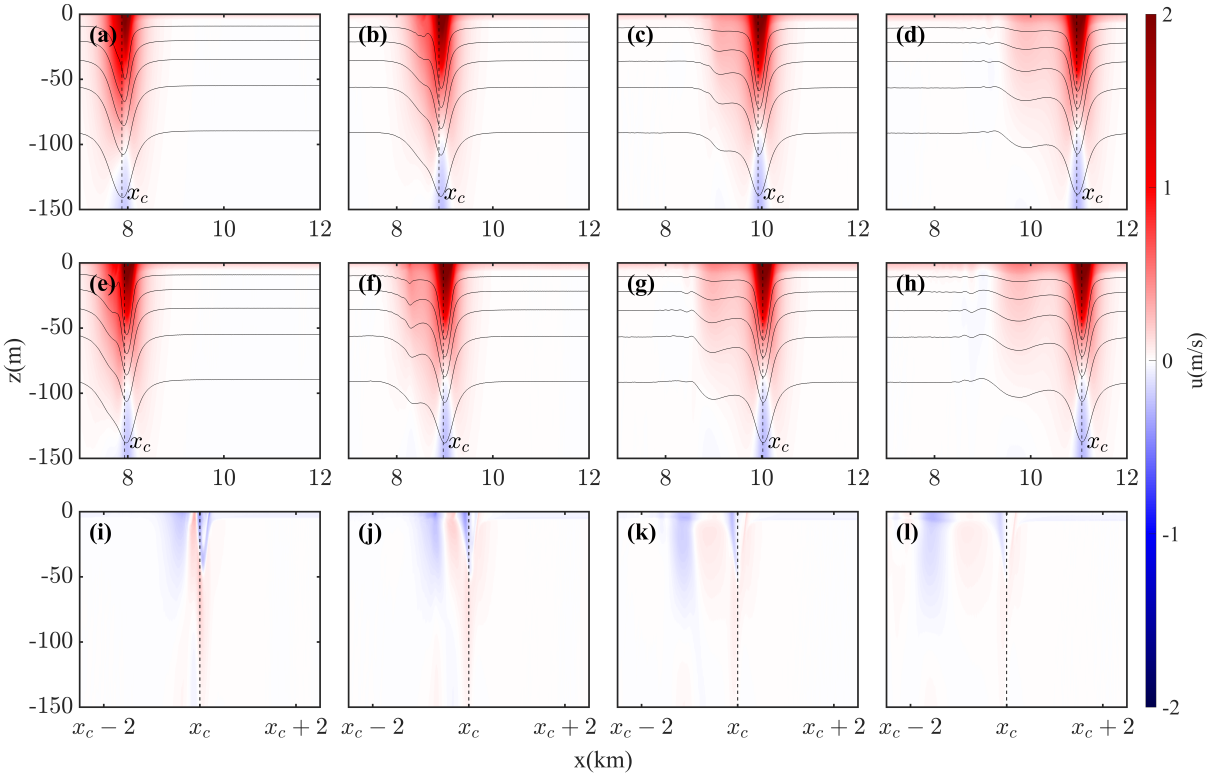


Figure 4.12: Comparison of cases P1-up and P1. The horizontal velocity component u in the top 150 m is shaded, with five density contours shown. Panels (a)-(d) show results from case P1-up at $t = 0.5, 0.7, 0.8, 1.0$ h. Panels (e)-(h) show results from case P1 at the same times. Panels (i)-(l) show the difference in u between the two cases, defined as $u_{\text{P1-up}} - u_{\text{P1}}$, after alignment by x_c.

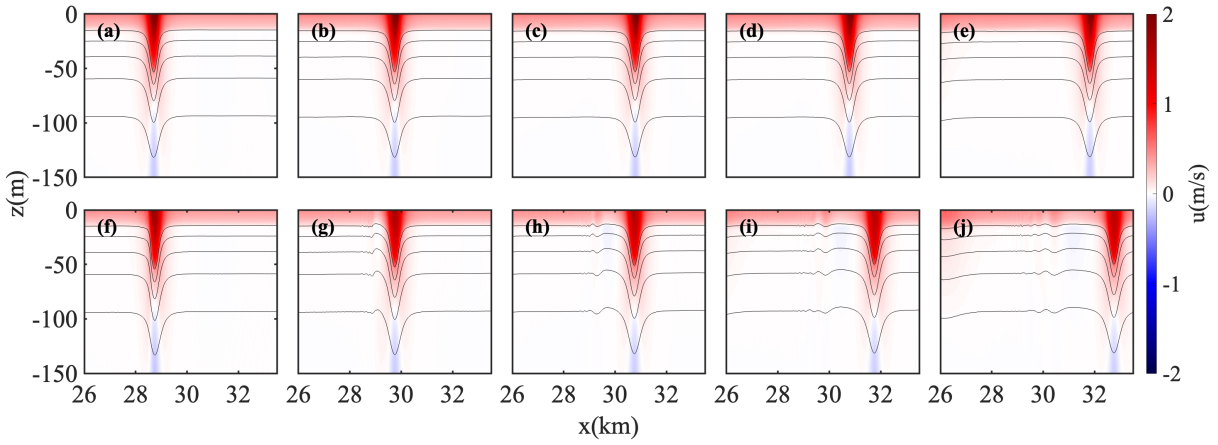


Figure 4.13: Comparison of cases P1-up and P1-up-down. The horizontal velocity component u in the top 150 m is shaded, with five density contours shown. Panels (a)-(e) show results from case P1-up at $t = 3.8, 4.0, 4.2, 4.3, 4.5$ h, while panels (f)-(j) show results from case P1-up-down at the same times.

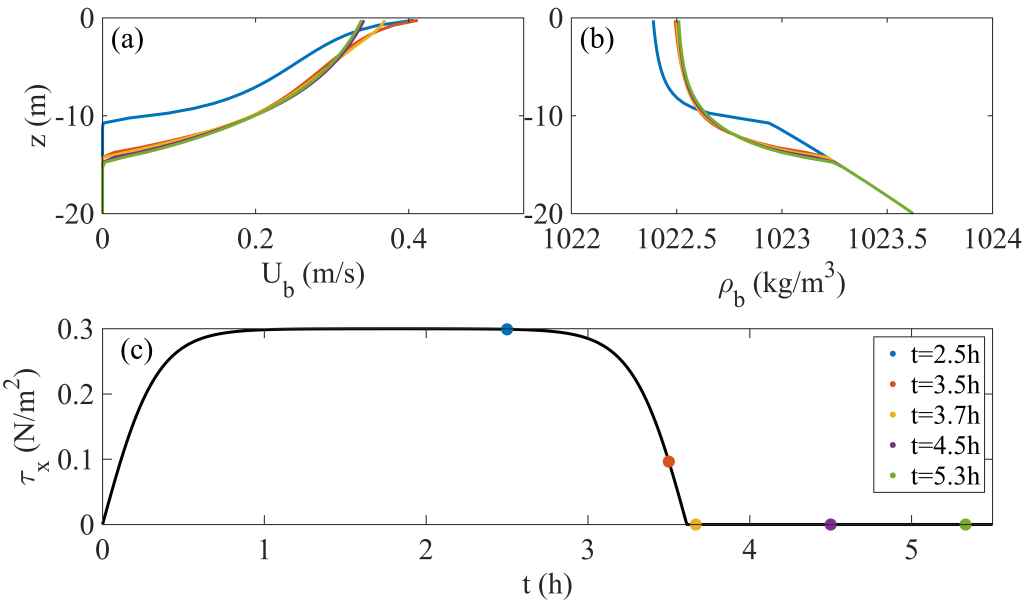


Figure 4.14: Evolution of the background conditions in Case P1-up-down: (a) background current profiles, $U_b(z)$; (b) background density profiles, $\rho_b(z)$; and (c) time evolution of wind stress, τ_x, with the times selected in panels (a) and (b) marked by dots.

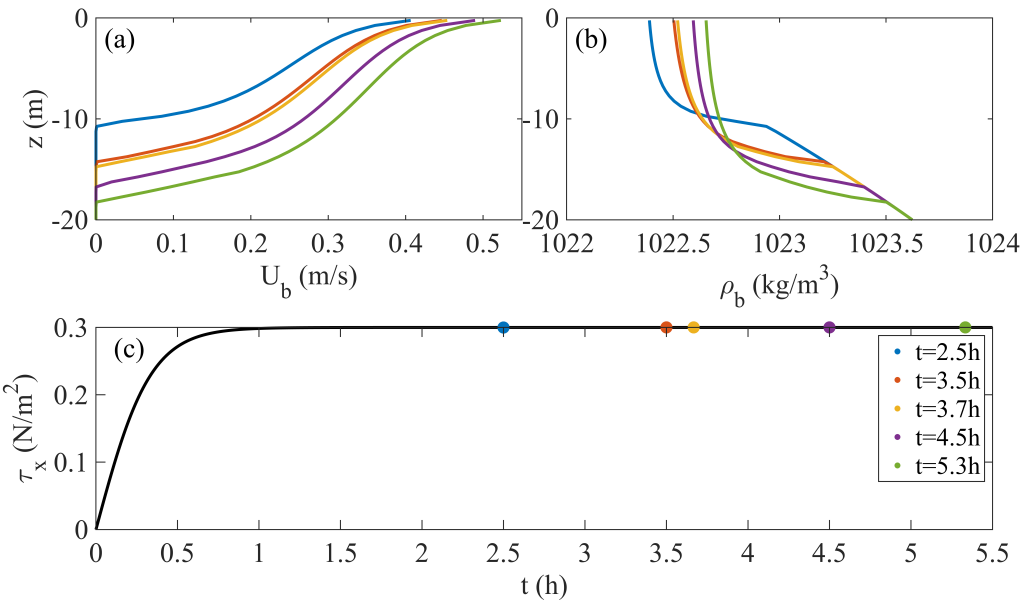


Figure 4.15: Same as Fig. 4.14, but for Case P1-up.

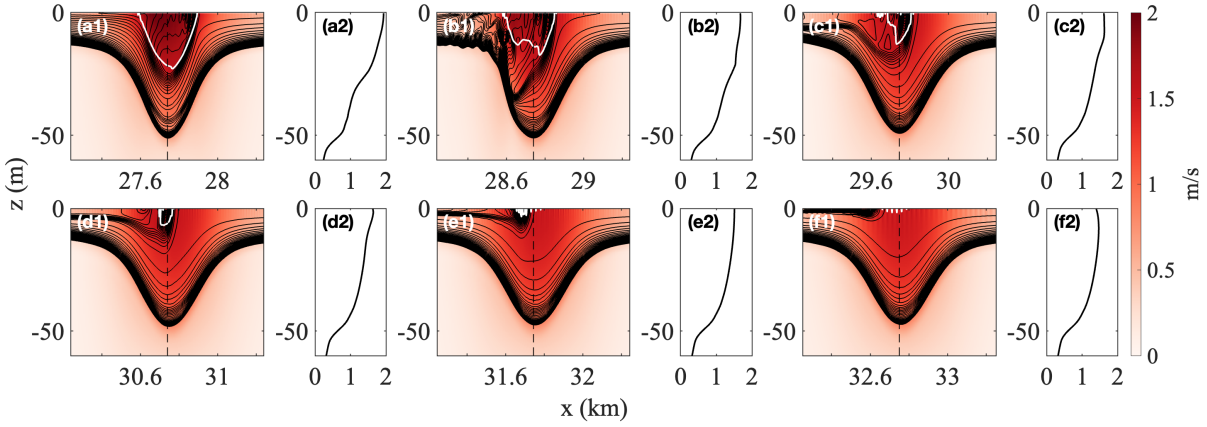


Figure 4.16: Close-up view of case P1-up-down during the wind-weakening period. Panels (a1)–(f1) show snapshots of u at $t = 3.7, 3.8, 4.0, 4.2, 4.3$, and 4.5 h in the upper 60 m, showing only the density contours near the surface as black lines. The white lines indicate where $u = c$. Panels (a2)–(f2) show the horizontal velocity profiles at the wave centre, u_c, with units of m/s.

Chapter 5

Discussion and Conclusions

In this study, we employed the MITgcm to investigate the influence of wind, through its effects on the background current and stratification, on the propagation of internal solitary waves. A commonly adopted parametrization for the effect of wind in the mixed layer, the KPP scheme, was employed throughout.

In the previous chapters, we first presented the results of the sensitivity experiments. These results show that a scheme like the KPP is necessary to represent the downward propagation of wind–induced momentum. When the KPP parametrization is enabled, the choice of grid resolution in MITgcm mainly affects the resolved scales. Finer grids are better able to capture wave fission and the resulting small-amplitude waves (Figure 3.4). The diffusion parameters had little effect on wave evolution unless the background vertical diffusivity was unrealistically high. Consequently, in the subsequent main experiments, the KPP parametrization was used as the vertical mixing scheme. The grid resolution was set to $\Delta x = 5$ m and $\Delta z = 0.5$ m in the upper domain, and the background diffusivities were set to $A_h = A_v = 10^{-5}$ m^{2}s^{-1}.

We then presented the results of the main suite of simulations. The first part of the analysis focused on the effects of constant wind stress. This included the positive wind forcing case, where the wave propagates concurrently with the wind, and the vorticity of the shear current also aligns with the wave-induced vorticity. It also included the negative wind forcing case, where the wave propagates in a counter-current direction, and the vorticity of the shear current is oriented in the opposite direction to the wave–induced vorticity.

Under positive wind forcing, the results show that wind-induced changes in the evolving background currents and stratification significantly alter the wave behaviour. More specifically, the wave initially undergoes a period of fission, after which it evolves into a

leading wave, followed by a secondary wave and weak trailing tails. Thereafter, its evolution becomes more gradual and is characterized primarily by a continuous decrease in amplitude. The initial fission can be interpreted as an adjustment to the development of strong near-surface shear. After this adjustment, fission does not recur, and trailing instabilities similar to those reported by Stastna et al. (2021) (their Figure 7) are not observed, even though our Figure 4.4 shows a persistent region where $|u| > |c|$ at the wave centre, which indicates convective instability. The absence of trailing instabilities may therefore be attributed to the representation of turbulent mixing by the KPP scheme. In particular, the high dissipation rate predicted near the wave centre suggests that the turbulent structures associated with overturning are not explicitly resolved in the simulation, but their dissipative effect is captured instead by the continuous decay of the wave amplitude.

The occurrence of a region where $|u| > |c|$ is commonly associated with the presence of closed streamlines in the wave frame and is referred to as a trapped core (Derzho and Grimshaw, 1997). The temporal variation in the thickness of the $|u| > |c|$ region can therefore be used as an indicator of changes in the core strength. The core persists because the near-surface vorticity of the background current does not increase substantially over time. Without KPP, the background vorticity would continue to increase, potentially causing the core vorticity to become sufficiently large to induce wave breaking, as shown in Fig. 3.2 (a)-(c). In the simulation P1, P2 and P3, the core thickness continuously decreases after the initial fission (Figure 4.5). This decreasing trend can be attributed to strong dissipation within the core. Lamb (2002) points out that the existence of a mixed layer is unfavorable for core formation, due to the reduced baroclinic generation. Therefore, the continuously deepening mixed layer under wind forcing may also contribute to this decrease. This process has not been investigated in depth in this study and remains a topic for future work.

Under negative wind forcing, the ISW propagates with a larger amplitude and greater stability than under positive wind forcing. A similar asymmetry in wave behavior under opposing shear conditions was observed by Stastna et al. (2021), who attributed it to the modification of the leading order balance between nonlinearity and dispersion by changes in the background shear. In addition to the wave structure being determined by the background stratification and current conditions, wind forcing in the present study can also inject momentum directly from the surface into the wave field, introduce turbulence, and thereby affect the wave evolution. The near-surface stratification at the centre of the wave is stronger under negative wind forcing than under positive wind forcing. This stronger stratification is less favorable for the downward transfer of turbulent fluxes from the surface layer. As a result, the parameterized turbulence level within the wave is reduced, which may also contribute to the larger wave amplitude observed under negative wind forcing.

Therefore, we conclude that wind direction plays a critical role in the response of ISWs to wind forcing through differences in the direction of wind-induced vorticity within the background shear currents. This finding calls into question the conclusion of Magalhaes et al. (2025), the only existing study that directly examines ISWs under wind forcing, that wind direction is not important for the combined effects of wind- and ISW-induced mixing. The discrepancy may arise because their study did not explicitly examine the influence of wind-induced shear currents on the wave field. In their MITgcm simulations, background currents were not applied because of the lack of near-surface velocity observations. Our results show that wind moving in the same direction as the wave enhances mixing around the wave centre, promotes regions of convective instability, and increases the propagation velocity. The role of wind direction should therefore receive greater attention when interpreting observational data.

After establishing the basic differences due to wind direction, we then presented the results of parameter-influence experiments. The first part of this work examines the effect of wind strength. The results show that wind strength does not fundamentally change wave evolution. The main effects are that stronger wind, when blowing in the same direction as the wave, causes the leading wave to propagate faster and its amplitude to decrease at a higher rate. This is attributed to the stronger turbulence induced by stronger wind and the associated higher dissipation rate.

The second part examines gradually ramping up wind, which may better represent real-life wind conditions. Compared with constant wind stress, gradually increasing wind stress leads to a slower evolution process, as expected. This implies that the influence of wind on ISW evolution is cumulative. Extending this finding to oceanic conditions, the wind history before observation can also affect the subsequent evolution of the wave. In contrast, gradually decreasing wind stress creates secondary instability and small amplitude trailing waves, as shown in Figure 4.13. This can be explained by the weakening of the near-surface background shear after the wind stops (Figure 4.14). Considering a shear-stratified fluid, stratification provides a wave-guide for gravity waves, whereas a background shear current provides a waveguide for vorticity waves (Stastna and Walter, 2014).The combined effects of these two mechanisms can lead to the formation of an ISW with a trapped vortex–rich core. When the shear weakens, the ocean state can no longer support the existence of a trapped core. Therefore, after the wind stops, the near surface shear decreases and the ISW adjusts from a trapped-core structure toward a new structure without closed density contours. This structural transition leads to the secondary instabilities observed in the simulation. These results further demonstrate the critical role of the background current structure in determining the wave structure. They also show that the existence of wind-induced shear depends on continuous wind momentum input. After the wind ceases, the

shear does not persist only through inertia. This is physically reasonable because eddy viscosity gradually weakens the shear once the wind input is removed.

The main limitations of the present study and possible directions for future work are summarized as follows. First, the background conditions considered here are simplified compared with those in the real ocean. Future work should consider more complex wind forcing, such as realistic two-dimensional wind fields, to better represent upper-ocean responses under typhoon conditions (Wu et al., 2008; Dare and McBride, 2011; Ma et al., 2025). The Coriolis effect should also be included, particularly for simulations over longer time scales. In addition, air temperature should be considered to examine the effects of surface heating and cooling. This is especially important when the air temperature is lower than the sea surface temperature, as surface cooling can generate convective instability near the ocean surface. This process is parameterized by the non-local terms in the KPP scheme, however these terms were not included in the present study. Including surface buoyancy forcing would therefore provide a more complete representation of wind-driven upper-ocean mixing and its influence on ISW evolution, at the cost of increasing complexity.

Second, applying the KPP scheme to ISWs also has limitations. The KPP scheme is a 1-D vertical mixing parameterization. In this study, it is mainly used to represent wind-induced vertical mixing and the downward transfer of wind-driven momentum. However, mixing induced by instabilities of ISWs interacting with shear currents is a different physical process. Such mixing cannot be represented by the current version of KPP. Previous studies suggest that instability associated with ISW evolution can be spatially asymmetric and may occur preferentially at the rear of the wave, as shown by Stastna et al. (2021) and Bolioudakis et al. (2026). Therefore, a possible adaptation for this process should further account for turbulence generated by unstable ISWs, as well as its horizontal variability.

More broadly, because KPP was originally designed for coarse-grid global models with an emphasis on computational efficiency, several aspects of the scheme are controversial when applied to high-resolution grids. First, it is a nonlocal scheme (Large et al., 1994). KPP diagnoses the boundary layer depth h and then constructs eddy viscosities and diffusivities using quantities at the boundary layer levels, such as surface fluxes and h. This nonlocal formulation makes it possible for the relationship between the prescribed eddy diffusivity structure and the local flow state to become detached. CATKE (Wagner et al., 2025), while also a first-order closure scheme, instead diagnoses eddy diffusivities from TKE and mixing lengths. Compared with KPP, this allows CATKE eddy diffusivities to evolve locally with the flow state, including variations in shear, stratification, and turbulence intensity. However, the scheme still requires further testing under complex forcing conditions. Second, another limitation of KPP is that it is essentially a first-order clo-

sure, meaning that the eddy diffusivities do not explicitly evolve turbulent fluxes. Recent work has applied higher-order closure approaches to better represent both diffusive and non-diffusive mixing in the ocean surface boundary layer (Garanaik et al., 2024, 2025). In addition, a commonly discussed issue is how to incorporate more physical processes into KPP. Upper-ocean processes that may influence mixing include Langmuir circulation (Craik and Leibovich, 1976), whose incorporation into KPP has been explored in several studies (Reichl et al., 2016; Li and Fox-Kemper, 2017), as well as surface wave breaking (Sullivan and McWilliams, 2010). Future studies should use improved versions of KPP that include these additional physical processes to simulate upper-ocean mixing under more realistic and complex forcing conditions.

Our work suggests that ISWs should be understood not only as isolated waves, but also as part of a coupled air-sea system. More specifically, the influence of surface forcings, such as heat flux and wind stress, on ISWs is important but often overlooked in the real ocean. These findings have important implications for both ocean observations and numerical modeling. From an observational perspective, these findings call for integrated atmospheric and oceanic measurements, including detailed observations of meteorological forcing and upper-ocean turbulence during the passage of ISWs. From a modeling perspective, advances in computational capacity have made high-resolution regional ocean simulations increasingly feasible in recent years. However, the current one-dimensional model cannot capture the asymmetric turbulent structure associated with ISWs. Therefore, future coastal ocean modeling will benefit from developing upper-ocean mixing schemes that account for horizontal variability relative to the wave centre of ISWs.

References

Alford, M. H., Peacock, T., MacKinnon, J. A., Nash, J. D., Buijsman, M. C., Centurioni, L. R., Chao, S.-Y., Chang, M.-H., Farmer, D. M., Fringer, O. B., Fu, K.-H., Gallacher, P. C., Graber, H. C., Helfrich, K. R., Jachec, S. M., Jackson, C. R., Klymak, J. M., Ko, D. S., Jan, S., Johnston, T. M. S., Legg, S., Lee, I.-H., Lien, R.-C., Mercier, M. J., Moum, J. N., Musgrave, R., Park, J.-H., Pickering, A. I., Pinkel, R., Rainville, L., Ramp, S. R., Rudnick, D. L., Sarkar, S., Scotti, A., Simmons, H. L., St Laurent, L. C., Venayagamoorthy, S. K., Wang, Y.-H., Wang, J., Yang, Y. J., Paluszkiewicz, T., and Tang, T.-Y. D. (2015). The formation and fate of internal waves in the South China Sea. *Nature*, 521(7550):65–69.

American Meteorological Society (2026). Tendency. Glossary of Meteorology.

Apel, J. R., Holbrook, J. R., Liu, A. K., and Tsai, J. J. (1985). The Sulu Sea internal soliton experiment. *Journal of Physical Oceanography*, 15(12):1625 – 1651.

Arakawa, A. and Lamb, V. R. (1977). Computational design of the basic dynamical processes of the UCLA general circulation model. In *General Circulation Models of the Atmosphere*, volume 17 of *Methods in Computational Physics: Advances in Research and Applications*, pages 173–265.

Bai, X., Lamb, K. G., Dong, C., Liu, A. K., Liu, Z., and Li, Q. (2019). Fission of shoaling internal waves on the northeastern shelf of the South China Sea. *Journal of Geophysical Research: Oceans*, 124(6):4529–4545.

Benney, D. J. (1966). Long non-linear waves in fluid flows. *Journal of Mathematics and Physics*, 45(1-4):52–63.

Boegman, L. and Stastna, M. (2019). Sediment resuspension and transport by internal solitary waves. *Annual Review of Fluid Mechanics*, 51:129–154.

Bolioudakis, T., Diamantopoulos, T., Diamessis, P. J., Lien, R.-C., Lamb, K. G., Rivera-Rosario, G., and Thomsen, G. N. (2026). Formation and evolution of turbulence in convectively unstable internal solitary waves of depression shoaling over gentle slopes in the South China Sea. *Journal of Physical Oceanography*, 56(3):533 – 559.

Cacchione, D. A., Pratson, L. F., and Ogston, A. S. (2002). The shaping of continental slopes by internal tides. *Science*, 296(5568):724–727.

Cai, S., Xie, J., and He, J. (2012). An overview of internal solitary waves in the South China Sea. *Surveys in Geophysics*, 33(5):927–943.

Cai, W.-J. (2011). Estuarine and coastal ocean carbon paradox: CO2 sinks or sites of terrestrial carbon incineration? *Annual Review of Marine Science*, 3(Volume 3, 2011):123–145.

Campin, J.-M., Adcroft, A., Hill, C., and Marshall, J. (2004). Conservation of properties in a free-surface model. *Ocean Modelling*, 6(3):221–244.

Chang, M.-H., Lien, R.-C., Tang, T., D'Asaro, E. A., and Yang, Y. J. (2021). Direct measurements reveal instabilities and turbulence within large amplitude internal solitary waves beneath the ocean. *Communications Earth & Environment*, 2:15.

Chen, X., Xu, G., Chen, Z., Zhu, L., and Cai, S. (2023). A study of the interaction between depression internal solitary waves and submerged floating tunnels in stratified fluids. *Applied Ocean Research*, 132:103455.

Choi, W. and Camassa, R. (1999). Fully nonlinear internal waves in a two-fluid system. *Journal of Fluid Mechanics*, 396:1–36.

Craik, A. D. D. and Leibovich, S. (1976). A rational model for Langmuir circulations. *Journal of Fluid Mechanics*, 73(3):401–426.

Dare, R. A. and McBride, J. L. (2011). Sea surface temperature response to tropical cyclones. *Monthly Weather Review*, 139(12):3798 – 3808.

de Boyer Montégut, C., Madec, G., Fischer, A. S., Lazar, A., and Iudicone, D. (2004). Mixed layer depth over the global ocean: An examination of profile data and a profile-based climatology. *Journal of Geophysical Research: Oceans*, 109(C12).

Derzho, O. G. and Grimshaw, R. (1997). Solitary waves with a vortex core in a shallow layer of stratified fluid. *Physics of Fluids*, 9(11):3378–3385.

Dunphy, M. and Lamb, K. (2014). Focusing and vertical mode scattering of the first mode internal tide by mesoscale eddy interaction. *Journal of Geophysical Research: Oceans*, 119.

Dunphy, M., Subich, C., and Stastna, M. (2011). Spectral methods for internal waves: indistinguishable density profiles and double-humped solitary waves. *Nonlinear Processes in Geophysics*, 18(3):351–358.

Ferrari, R. and Boccaletti, G. (2004). Eddy-mixed layer interactions in the ocean. *Oceanography*, 17.

Foltz, G. R. (2019). Wind- and buoyancy-forced upper ocean. In *Encyclopedia of Ocean Sciences*, pages 113–121. Academic Press, Oxford, third edition edition.

Garanaik, A., Li, Y., Moreno-Comstock, S., Li, Q., van Roekel, L., and Pearson, B. (2025). Developing a new plume-based non-local turbulence closure scheme under complex oceanic forcing. In *Division of Fluid Dynamics Annual Meeting 2025*. APS.

Garanaik, A., Pereira, F. S., Smith, K., Robey, R., Li, Q., Pearson, B., and Van Roekel, L. (2024). A new hybrid mass-flux/high-order turbulence closure for ocean vertical mixing. *Journal of Advances in Modeling Earth Systems*, 16(1):e2023MS003846.

Gelderloos, R., Szalay, A. S., Haine, T. W. N., and Lemson, G. (2016). A fast algorithm for neutrally-buoyant Lagrangian particles in numerical ocean modeling. In 2016 IEEE 12th International Conference on e-Science.

Gerkema, T. and Zimmerman, J. T. F. (1995). Generation of nonlinear internal tides and solitary waves. *Journal of Physical Oceanography*, 25(6):1081 – 1094.

Gill, A. E. (1982). Chapter 9 - forced motion. In *Atmosphere—Ocean Dynamics*, volume 30 of *International Geophysics*, pages 317–370. Academic Press.

Glenn, S. M., Miles, T. N., Seroka, G. N., Xu, Y., Forney, R. K., Yu, F., Roarty, H., Schofield, O., and Kohut, J. (2016). Stratified coastal ocean interactions with tropical cyclones. *Nature Communications*, 7(1):10887.

Gregg, M. C. (2021). Chapter 8. In *Ocean Mixing*, pages 283–318. Cambridge University Press, Cambridge.

Grimshaw, R., Pelinovsky, E., and Talipova, T. (2007). Modelling internal solitary waves in the coastal ocean. *Surveys in Geophysics*, 28:273–298.

Guo, C. and Chen, X. (2014). A review of internal solitary wave dynamics in the northern South China Sea. *Progress in Oceanography*, 121:7–23. Recent Developments In Oceanography of the Asian Marginal Seas.

Guo, D., Zhan, P., and Hoteit, I. (2021). Three-dimensional simulation of shoaling internal solitary waves and their influence on particle transport in the Southern Red Sea. *Journal of Geophysical Research: Oceans*, 126(4):e2020JC016335.

Helfrich, K. R. and Melville, W. (1986). On long nonlinear internal waves over slope-shelf topography. *Journal of Fluid Mechanics*, 167:285–308.

Helfrich, K. R. and Melville, W. K. (2006). Long nonlinear internal waves. *Annual Review of Fluid Mechanics*, 38(Volume 38, 2006):395–425.

Jackson, C. (2007). Internal wave detection using the moderate resolution imaging spectroradiometer (*modis*). *Journal of Geophysical Research: Oceans*, 112(C11).

Kunze, E. (2017). Internal-wave-driven mixing: Global geography and budgets. *Journal of Physical Oceanography*, 47(6):1325 – 1345.

Lamb, K. G. (2002). A numerical investigation of solitary internal waves with trapped cores formed via shoaling. *Journal of Fluid Mechanics*, 451:109–144.

Lamb, K. G. (2013). Internal wave breaking and dissipation mechanisms on the continental slope/shelf. *Annual Review of Fluid Mechanics*, 46.

Lamb, K. G. and Farmer, D. (2011). Instabilities in an internal solitary-like wave on the Oregon Shelf. *Journal of Physical Oceanography*, 41(1):67 – 87.

Lamb, K. G., Lien, R.-C., and Diamessis, P. J. (2019). Internal solitary waves and mixing. In *Encyclopedia of Ocean Sciences*, pages 533–541. Academic Press, Oxford, third edition edition.

Lamb, K. G. and Yan, L. (1996). The evolution of internal wave undular bores: comparisons of a fully nonlinear numerical model with weakly nonlinear theory. *Journal of Physical Oceanography*, 26(12):2712–2734.

Large, W. G., McWilliams, J. C., and Doney, S. C. (1994). Oceanic vertical mixing: A review and a model with a nonlocal boundary layer parameterization. *Reviews of Geophysics*, 32(4):363–403.

Large, W. G. and Pond, S. (1981). Open ocean momentum flux measurements in moderate to strong winds. *Journal of Physical Oceanography*, 11(3):324 – 336.

Lee, C.-Y. and Beardsley, R. C. (1974). The generation of long nonlinear internal waves in a weakly stratified shear flow. *Journal of Geophysical Research*, 79(3):453–462.

Li, Q. and Fox-Kemper, B. (2017). Assessing the effects of langmuir turbulence on the entrainment buoyancy flux in the ocean surface boundary layer. *Journal of Physical Oceanography*, 47(12):2863 – 2886.

Lien, R.-C., D'Asaro, E. A., Henyey, F., Chang, M.-H., Tang, T.-Y., and Yang, Y.-J. (2012). Trapped core formation within a shoaling nonlinear internal wave. *Journal of Physical Oceanography*, 42(4):511–525.

Long, R. R. (1953). Some aspects of the flow of stratified fluids: I. A theoretical investigation. *Tellus*, 5(1):42–58.

Ma, T., Yu, W. D., Speich, S., et al. (2025). Philippine Archipelago and South China Sea monsoon plus ocean cooling buffer Northwestern Pacific super typhoons. *Nature Communications*, 16:7395.

Magalhaes, J. M., Coubard, M. J., da Silva, J. C., Buijsman, M. C., Santos, A. I., Amorim, A., and Oliveira, P. B. (2025). Shear instabilities in internal solitary waves under high and low-wind regimes. *Continental Shelf Research*, 295:105561.

Marshall, J., Adcroft, A., Hill, C., Perelman, L., and Heisey, C. (1997a). A finite-volume, incompressible Navier Stokes model for studies of the ocean on parallel computers. *Journal of Geophysical Research: Oceans*, 102(C3):5753–5766.

Marshall, J., Hill, C., Perelman, L., and Adcroft, A. (1997b). Hydrostatic, quasi-hydrostatic, and nonhydrostatic ocean modeling. *Journal of Geophysical Research: Oceans*, 102(C3):5733–5752.

Mathis, M., Logemann, K., Maerz, J., Lacroix, F., Hagemann, S., Chegini, F., Ramme, L., Ilyina, T., Korn, P., and Schrum, C. (2022). Seamless integration of the coastal ocean in global marine carbon cycle modeling. *Journal of Advances in Modeling Earth Systems*, 14(8).

McWilliams, J. C. (2006). *Fundamentals of geophysical fluid dynamics*. Cambridge University Press.

Miles, J. (1994). On transversely isotropic eddy viscosity. *Journal of Physical Oceanography*, 24(5):1077 – 1079.

Miles, T., Seroka, G., and Glenn, S. (2017). Coastal ocean circulation during *hurricanesandy*. *Journal of Geophysical Research: Oceans*, 122(9):7095–7114.

Miyata, M. (1985). An internal solitary wave of large amplitude. *La mer*, 23(2):43–48.

Miyata, M. (1988). Long internal waves of large amplitude. In Horikawa, K. and Maruo, H., editors, *Nonlinear Water Waves*, pages 399–406. Springer, Berlin, Heidelberg.

Munk, W. and Wunsch, C. (1998). Abyssal recipes II: energetics of tidal and wind mixing. *Deep Sea Research Part I: Oceanographic Research Papers*, 45(12):1977–2010.

Pickett, M. H. and Paduan, J. D. (2003). Ekman transport and pumping in the California Current based on the U.S. Navy's high-resolution atmospheric model (COAMPS). *Journal of Geophysical Research: Oceans*, 108(C10).

Press, W., Teukolsky, S., Vetterling, W., and Flannery, B. (1986). *Numerical Recipes*. Cambridge University Press.

Price, J. F., Weller, R. A., and Pinkel, R. (1986). Diurnal cycling: Observations and models of the upper ocean response to diurnal heating, cooling, and wind mixing. *Journal of Geophysical Research: Oceans*, 91(C7):8411–8427.

Qi, J., Chen, C., Beardsley, R. C., Perrie, W., Cowles, G. W., and Lai, Z. (2009). An unstructured-grid finite-volume surface wave model (FVCOM-SWAVE): Implementation, validations and applications. *Ocean Modelling*, 28(1):153–166.

Regnier, P.and Friedlingstein, P. and Ciais, P. (2013). Anthropogenic perturbation of the carbon fluxes from land to ocean. *Nature Geoscience*, 6:597–607.

Reichl, B. G., Wang, D., Hara, T., Ginis, I., and Kukulka, T. (2016). Langmuir turbulence parameterization in tropical cyclone conditions. *Journal of Physical Oceanography*, 46(3):863 – 886.

Stastna, M. (2022). *Internal Waves in the Ocean: Theory and Practice*. Surveys and Tutorials in the Applied Mathematical Sciences. Springer International Publishing.

Stastna, M., Coutino, A., and Walter, R. K. (2021). The effect of strong shear on internal solitary-like waves. *Nonlinear Processes in Geophysics*, 28(4):585–598.

Stastna, M. and Lamb, K. G. (2002). Large fully nonlinear internal solitary waves: The effect of background current. *Physics of Fluids*, 14(9):2987–2999.

Stastna, M. and Legare, S. (2024). Simulations of shoaling large-amplitude internal waves: perspectives and outlook. *Flow*, 4:E11.

Stastna, M. and Walter, R. (2014). Transcritical generation of nonlinear internal waves in the presence of background shear flow. *Physics of Fluids*, 26(8):086601.

Sullivan, P. P. and McWilliams, J. C. (2010). Dynamics of winds and currents coupled to surface waves. *Annual Review of Fluid Mechanics*, 42:19–42.

Thorpe, S. A. (2005). *The upper ocean boundary layer*, page 228–268. Cambridge University Press.

Troen, I. and Mahrt, L. (1986). A simple model of the atmospheric boundary layer; sensitivity to surface evaporation. *Boundary-Layer Meteorology*, 37:129–148.

Wagner, G. L., Hillier, A., Constantinou, N. C., Silvestri, S., Souza, A., Burns, K. J., Hill, C., Campin, J.-M., Marshall, J., and Ferrari, R. (2025). Formulation and calibration of CATKE, a one-equation parameterization for microscale ocean mixing. *Journal of Advances in Modeling Earth Systems*, 17(4).

Walter, R. K., Stastna, M., Woodson, C. B., and Monismith, S. G. (2016). Observations of nonlinear internal waves at a persistent coastal upwelling front. *Continental Shelf Research*, 117:100–117.

Whalen, C. B., de Lavergne, C., Naveira Garabato, A. C., Melet, A., Fer, I., Garuba, O., Brearley, J., Gille, S. T., Griffies, S. M., Hallberg, R., Legg, S., and Nikurashin, M. (2020). Internal wave-driven mixing: governing processes and consequences for climate. *Nature Reviews Earth & Environment*, 1:606–621.

Wu, C.-R., Chang, Y.-L., Oey, L.-Y., Chang, C.-W. J., and Hsin, Y.-C. (2008). Air-sea interaction between tropical cyclone Nari and Kuroshio. *Geophysical Research Letters*, 35(12).

Xie, J., He, Y., Chen, Z., Xu, J., and Cai, S. (2015). Simulations of internal solitary wave interactions with mesoscale eddies in the Northeastern South China Sea. *Journal of Physical Oceanography*, 45(12):2959 – 2978.

Yu, L. and Weller, R. A. (2007). Objectively analyzed air–sea heat fluxes for the global ice-free oceans (1981–2005). *Bulletin of the American Meteorological Society*, 88(4):527 – 540.

Zhao, S., Hu, H., Ouahsine, A., Lu, H., Li, Z., Yuan, Z., and Du, P. (2025). Advances of complex marine environmental influences on underwater vehicles. *Journal of Marine Science and Engineering*, 13(7).

Zhao, Z., Klemas, V. V., Zheng, Q., and Yan, X.-H. (2003). Satellite observation of internal solitary waves converting polarity. *Geophysical Research Letters*, 30(19).

Zou, P., Bricker, J. D., and Uijttewaal, W. S. (2020). Impacts of extreme events on hydrodynamic characteristics of a submerged floating tunnel. *Ocean Engineering*, 218:108221.